UNIVERSITY OF CALIFORNIA, MERCED

Phase-Templated Self-Assembly of Nanoparticles in Confined Liquid Crystal

A dissertation submitted in partial satisfaction of the requirements for the degree
Doctor of Philosophy

in

Physics

by

Charles Nathan Melton

Committee in charge:

Professor Ajay Gopinathan, Chair
Professor Linda Hirst
Professor Jay Sharping
Professor Benjamin Stokes

2018

The Dissertation of Charles Nathan Melton is approved, and is acceptable in quality and form for publication on microfilm and electronically:

Jay E. Sharping

Benjamin Stokes

Linda Hirst

Ajay Gopinathan , Chair

University of California, Merced

2018

Dedication

To my mother…

Table of Contents

Lists of Figures

List of Tables

Acknowledgements

There are too many people to thank for this opportunity. My largest thanks to my advisor, Professor Linda Hirst. Without here guidance, this would have not been possible. I am also extremely grateful to my committee members: Professors Ajay Gopinathan, Jay Sharping, and Benjamin Stokes. All have been extremely helpful towards my research with the advice they have given. I am also grateful towards Robin Selinger of Kent State, who has been a fantastic mentor to me regarding my computational work. To my labmates Joseph Lopes, Amanda Tan, Sheida Riahinasab: thank you all for all you have done for me. And finally, thank you to all the friends I've made along this journey: Stephen Dale, Al Castelli, Andrew Jacobs, Joshua Casara, Melissa Michell, Alison Huff, Rodolfo Lopez, and to all the others who would take up several pages.

Thank you to my family who have been a massive support. Mom, Nana, Aunt Marty, Joe, Nick, Tony, Sam, Chase, Blake, Uncle Lynn, Aunt Terry: thank you all.

I am also extremely grateful for the funding I have received from NSF to help fund this research.

Permission has been granted from CRC Press to use copyrighted material in this dissertation. The permission was obtained electronically from www.copyright.com. Unless stated, all other figures were generated by Charles Nathan Melton.

Curriculum Vitae

Education

2018	Ph.D., Physics, University of California Merced
2012	M.S., Physics, University of Memphis
2010	B.S., Physics, Christian Brothers University

Work Experience

Experimental researcher in the Hirst Soft Matter Physics Lab, specializing in liquid crystals / nanoparticle composites and lipid bilayers

Theoretical work for the Hirst Soft Matter Physics Lab, focusing on spin model systems, topological defects, and phase separation

Facilitated various discussion sections and laboratory experiments as a Teaching Assistant in various mathematical and physics courses

Laboratory Skills

Fluorescent Microscopy
Confocal Microscopy
Electorformation of Lipid Vesicles
X-Ray beamline experience – SSRL(Stanford) beam line and Advanced Light Source (Lawrence-Berkeley National Laboratory)
Experienced coding skills: Python, Mathematica
Elementary coding skills: C++, Matlab

Awards

UC Merced Physics Summer Fellowship Award (2014, 2015, 2016, 2017)
UC Merced Physics Travel Award (2014, 2015, 2016, 2017, 2018)

Conference and Seminar Presentations

APS Far West Conference, University of Nevada, Reno. "Particles at the Interface of Oil and Water: Topological Defects Produced by Anisotropic Particles" – Talk, October 2014

APS March Meeting, San Antonio, Texas. "Topological Defects in Liquid Crystal: Understanding Defect and Curvature Coupling" – Talk, March 2015

APS Far West Conference, California State Long Beach. "Quantum Dot Cluster Self-Assembly via Topological Defects in Spherical and Planar Geometries of Liquid Crystal" – Talk, October 2015

International Liquid Crystal Conference, Kent State, Kent, OH. "Utilizing Phase Front Propagation in Liquid Crystal Droplets to Control Quantum Dot Self-Assembly" – Poster, August 2016

APS Far West Conference, UC Davis, Davis, CA. "Utilizing Phase Front Propagation in Liquid Crystal Droplets to Control Quantum Dot Self-Assembly" – Talk, October 2016

APS March Meeting, New Orleans, LA. "Quantum Dot Self-Assembly in Liquid Crystal Droplets" – Talk, March 2017

Liquid Crystal Gordon Research Conference, Biddeford, ME. "Quantum Dot Self-Assembly in Liquid Crystal Droplets" – Poster, June 2017

APS March Meeting, Los Angeles, CA. "Computational Study of a Nanoparticle-Rich Domain Formation in a Nematic Liquid Crystal" – Talk, March 2018

Publications

1. Charles N. Melton, Sheida T. Riahinasab, Amir Keshavarz, Benjamin J. Stokes, and Linda S. Hirst. Characterization of Quantum Dot Micro-Shells formed in Liquid Crystal Droplets. In Preparation.

2. Charles N. Melton, Sheida T. Riahinasab, Amir Keshavarz, Benjamin J. Stokes, and Linda S. Hirst. Phase Transition-Driven Nanoparticle Assembly in Liquid Crystal Droplets. Nanomaterials, **8**, 2018, DOI: 10.3390/nano8030146

3. Sheida T. Riahinasab, Amir Keshavarz, Charles N. Melton, Ahmed Elbaradei, Gabrielle I. Warren, Robin L.B. Selinger, Benjamin J. Stokes, and Linda S. Hirst. Solid Nanoparticle Foam Formed by Double Nematic Nucleation and Growth. In Preparation.

4. Linda S. Hirst, Sheida T. Riahinasab, and Charles N. Melton. Liquid Crystal Composites as a Route to 3D Nanoparticle Assembly. SPIE Newsroom, 16 June 2017. DOI: 10.1117/2.1201702.00686

5. Alison Huff, Charles N. Melton, Linda S. Hirst, and Jay E. Sharping. Stability and instability for low refractive-index-contrast particle trapping in a dual-beam optical trap. Biomedical Optics Express, **6**, 2015.

6. F. Sabri. J. Marchetta, M. Redding, J. Habenicht, T. Chung, C. Melton, C. Hatch, R. Lirette. Effect of Surface Plasma Treatments on the Adhesion of Mars JSC 1 Simulant Dust to RTV 655, RTV 615, and Sylgard 184. PlosOne, **7**, 2012.

7. Charles Nathan Melton. Optical Detection of Surface Damage of RTV 655 using a Laser Speckle Contrast Technique – A Feasibility Study. Master's Thesis, 2012.

Abstract

Phase-Templated Self-Assembly of Nanoparticles in Confined Liquid Crystal
Charles Nathan Melton
University of California, Merced, 2018
Committee Chair: Ajay Gopinathan

The self-assembly of nanoparticles by an anisotropic fluid allows for the study of fascinating phenomena and the potential to assemble structures that can be used for a variety of industrial and biological applications. Here, we use a nematic liquid crystal to drive the self-assembly of quantum dots in confined geometries. The quantum dots have been modified with a special mesogenic ligand that aids in dispersion into the liquid crystal host.

By confining the liquid crystal to a certain geometry, we can assemble nanoparticle structures at defined locations, as the geometry forces the formation of topological defects in certain areas. Particles gather at topological defects to lower the free energy of the system, and so we utilize this fact to gain spatial control over the self-assembly process. We also use the isotropic-nematic phase transition of the liquid crystal to direct the self-assembly by forcing the particle to non-energetically favorable locations, as spatial control is one of the current hurdles in self-assembly research. Using droplet geometry, we successfully form nanoparticle cluster and hollow micro-shells at defined locations in the liquid crystal. The phase transition sweeps up the particles in a process to ballistic aggregation, so we characterize the fractal nature of these aggregates, quantifying their packing dimension to be 2.5.

Finally, we have developed a model that replicates the particle-rich domains in a phase-changing nematic liquid crystal. Using a spin model that exhibits a first-order phase transition combined with the Cahn Hillard equation adjusted with a new driving term proportional to the nematic order parameter, we study the effect of cooling rate of the liquid crystal and how that changes particle domain size. We recover a linear relationship, showing that as cooling rate is increased, particle domain size decreases. In conclusion, these simulations have helped further the understanding of phase-transition driven self-assembly.

Chapter 1

Introduction

1.1 Self-Assembly Overview

Self-assembly is a process that has led to the development of many novel materials and devices [1-5]. Of interest in recent research is the self-assembly of nanoparticles, particularly quantum dots, which have been building blocks for numerous applications [6-10]. These aren't the only materials of interest however. Other materials range from simple particle ranging in size to complex biological molecules [11-13]. There are many forces that can drive self-assembly. Kinetics of particles [14, 15], hydrophobic and hydrophilic effects of molecular compounds [16], and forces due to a surrounding medium [17,18]: all can drive the formation of new structures from constituent materials. In general, several types of self-assembled structures have been constructed in different media such as linear chains, clusters, and structured arrays [19-22].

One major advantage of forming materials through a self-assembly process is its highly tunable nature. The concept of self-assembly is straight forward: one material (the constituent) is acted on by outside forces (the host material) and these forces drive the self-assembly. These forces vary from case to case, from molecules introduced to start an assembly process, to repulsion potentials between constituents, to direct interaction with the host material. The end results of these processes can be finely tuned by several parameters, such as temperature, concentration, and formation method. For example: lipids in water.

Lipids are a biological molecule that contain a hydrophilic head group and a hydrophobic tail group, shown in Figure 1a. This tail group can be either saturated or unsaturated, meaning the tail group consists of either single carbon bonds or at least one double carbon bond, respectively. Upon putting lipids into an aqueous solution, water molecules are unable to form hydrogen bonds with the hydrophobic tails, thus limiting the total number of conformations water molecules can explore. To allow for the exploration of as many configurations as

possible, the lipids will arrange themselves with their hydrophilic head groups towards the solution, enclosing the hydrophobic tail groups away from the solution, thus maximizing the entropy of the system. A bilayer consists of lipid that has the head groups face towards the aqueous solution and the tail groups gathered together between the two head groups as shown in Figure 1b. These bilayer formations can be tuned to produce unique structure not usually seen in nature, such as bilayer disks [23].

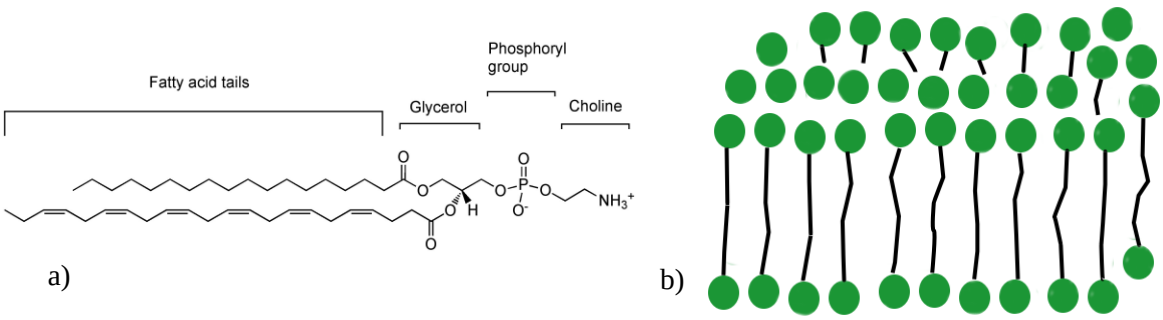

Figure 1 a) Schematic of a common lipid acquired from [16]. b) is a diagram of an assembled lipid bilayer.

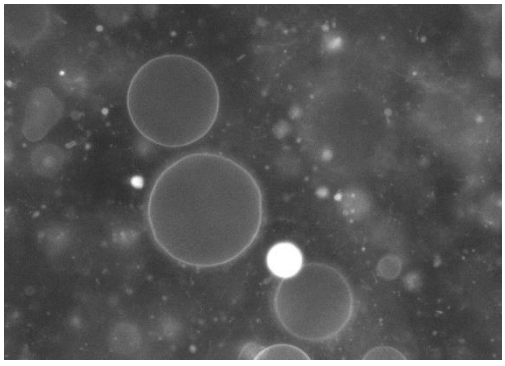

Figure 2: Fluorescence microscopy image of spherical lipid vesicles in water.

While lipids are useful for studying biological applications, the focus of this dissertation is to study the self-assembly of nanoparticles. More specifically: quantum dots. Self-assembled particles may exhibit collective electronic,

photonic, or magnetic properties not seen in isolated particles [24,25]. By inserting quantum dots into an anisotropic material, in this case a nematic liquid crystal, elastic forces will drive the self-assembly of particle structures. Liquid crystals will be discussed in the following section.

1.2 Liquid Crystal Overview

A liquid crystal is a material that exhibits a stable thermodynamic phase between the liquid and crystalline phases and has both short-range molecular order and fluid-like properties. Liquid crystal molecules can come in a variety of shapes, such as rods and disks [26, 27]. These different shapes give rise to a variety of different liquid crystal phases and bulk material behavior. Rods and disks have varying degrees of anisotropy, depending on which direction the molecule is viewed. This anisotropy gives rise to the famous birefringence patterns liquid crystals are known for [28]. An example of this birefringence pattern is shown in Figure 3a.

Liquid crystals can have many different phases depending on molecular shape and orientation. One of the most known is the nematic liquid crystal. A nematic liquid crystal is a material whose molecular structure has a high aspect ratio (rod shaped or disc shaped). A common nematic liquid crystal used in many experiments is 4-cyano-4'-pentylbiphenyl (5CB). The molecular structure of 5CB is shown in Figure 3b.

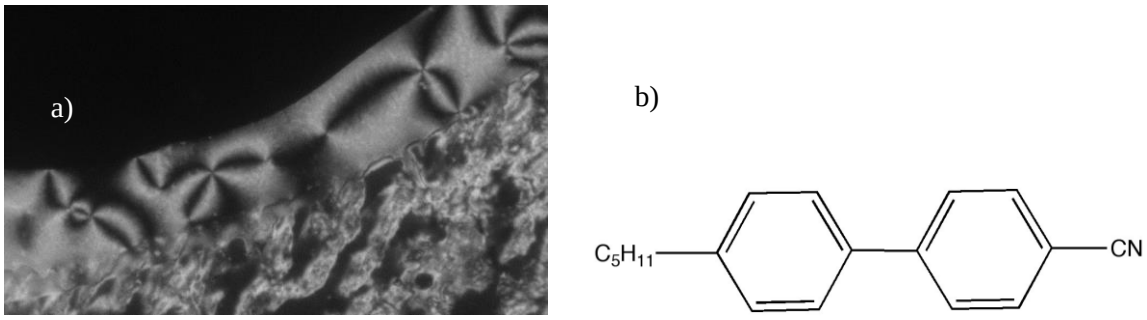

Figure 3: a) Birefringence textures of a nematic liquid crystal. b) is the molecular structure of 5CB, obtained from [16].

At a certain temperature known as the isotropic-nematic phase transition temperature, 5CB undergoes a phase change from a liquid state to a nematic liquid crystal state. Specifically, for 5CB this is 35 °C [29]. In the nematic state molecules are, on average, aligned in a common direction. This direction of alignment is designated by a unit vector, **n**, which is called the director [30]. This alignment is local only; a bulk sample of nematic material will have random orientation over the whole, but locally will have orientational order. A schematic showing how these molecules align in each specific state (liquid, liquid crystal, and crystalline) is shown in Figure 4.

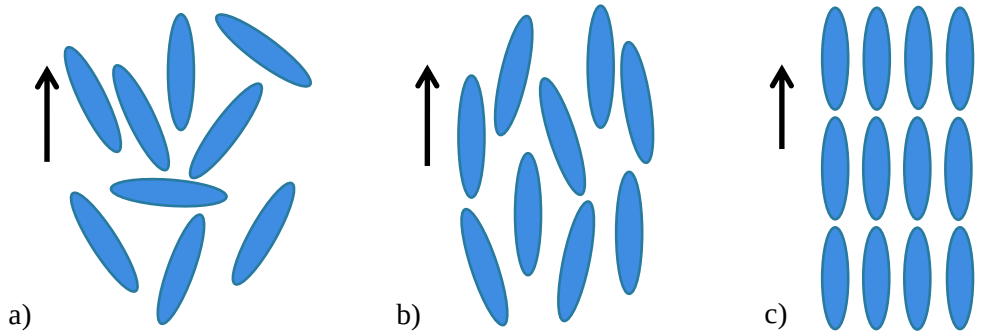

Figure 4: Schematic of the distinct phases of 5CB. a) is the isotropic phase. b) is the nematic phase, and c) is the crystalline phase.

Nematic liquid crystals are known to easily align with applied electric fields [31, 32]. This is due to the permanent electric dipole formed from ends of the nematic liquid crystal having opposite charges. This property has led the nematic to be used for a variety of applications, such as lenses [33], optical switches [34], and displays [35].

Other types of liquid crystals include smectic liquid crystals. Smectics are like nematics in terms of molecular structure, but differ in molecular orientation. Smectic liquid crystals have layers of rod-like molecules stacked on one another [36]. These layers can be aligned in the same direction producing a phase called

Smectic-A, while the molecules making up the layers can become tilted, producing the Smectic-C phase. Another common type of liquid crystal is a cholesteric liquid crystal. In a cholesteric phase, molecules are aligned in each plane, and exhibit a rotation as you go through the sample (Figure 5). These can be prepared by taking a nematic liquid crystal and introducing a chiral derivative [37]. The distance it takes the layers to undergo one full rotation is called the pitch. The pitch of a cholesteric liquid crystal can change based on properties such as concentration and temperature. Color changing thermometers and mood rings consist of a cholesteric liquid crystal, as the visible color is a product of light incident with the pitch. The changing pitches combined with doped cholesterics that affect either absorbed or emitted wavelengths produces a liquid crystal laser [38, 39].

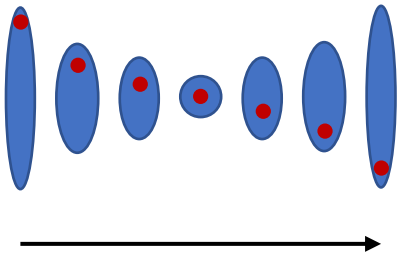

Figure 5: Schematic of the half-pitch of a cholesteric liquid crystal. The red dot represents the direction of rotation.

This has been a general overview of liquid crystals. While liquid crystals themselves have unique and interesting properties, they have been an important tool in furthering self-assembly research. Being able to control factors such as molecular orientation, phase change behavior, and various other parameters has led to fascinating results in the field of self-assembly. These topics will be discussed in the next section, and this work will focus simply on nematic liquid crystals.

1.3 Liquid Crystal Driven Self-Assembly

Liquid crystals have been shown to be a host material that results in successful self-assembly [40-42]. A variety of materials have been successfully self-assembled into structures. These range from biological compounds, to quantum dots, to colloidal particles. A few properties of the liquid crystal that drive the self-assembly process are molecular orientation, elastic forces, phase changes.

The assembly of colloidal particles in liquid crystal has been the focus of much research [11-13, 17-19]. Assembling very small particles (~10 nm in diameter) proves more of a challenge since the particles are subjected to strong Brownian fluctuations where the size of the particle approaches that of solvent molecules. Liquid crystals have proven to be a useful tool in limiting these strong fluctuations due to the inherent elastic properties of the host material [3].

Molecular orientation plays a large role in self-assembly in a liquid crystal host. As stated in Section 1.2, nematic liquid crystals tend to align in a general direction. This produces what can be considered as an ordered fluid. There are occasions, however, where the nematic molecules do not align in the same directions over small distances. This results in a degree of ordered frustration which is called a topological defect. It has been shown extensively that nanoparticle tend to gather at topological defects [43]. In a 3D bulk, topological defects may be connected by disinclination lines through the liquid crystal [44]. Particles are known to gather in these lines as well, forming connected arrays of particles. Particles collecting at topological defects are driven there due to the next topic of liquid crystal self-assembly: elastic forces.

As nematic liquid crystal molecules prefer to align in a general direction. Consider the insertion of a particle into an aligned liquid crystal. The liquid crystal can no longer locally align and will have to use energy to deform the director field around the particle. This elastic deformation is governed by the Frank elastic energy which is of the form $F = \frac{1}{2}kx^2$ [45], where x is a term which describes the deformation. Entropically, this also restricts the number of conformations the material can explore by forcing molecules into particular arrangements. To

decrease this energy cost, the system will drive the particles to areas which already have an increase in energy via Brownian motion: the topological defects.

The final method of self-assembly in a liquid-crystal to be considered is the induced phase change. Having the phase change govern self-assembly is known as phase templating. This is a more recently discovered phenomenon and has led to the development of new structures such as hollow quantum dot micro-shells and hollow networks when the particles have been functionalized with a carefully designed ligand [46-49]. In this method of self-assembly, particles are swept up via the isotropic-nematic phase front (the direction of the phase change in the bulk). Upon being swept up by the phase front, clusters and structures are formed. Due to ligand-ligand interactions between particles are large enough that nematic forces cannot move the structures around, and so topological defects form at these structure locations.

These three methods of self-assembly are reliable methods for creating unique, stable structures in a liquid crystal environment. There is precise control over how large and what types of structures can form. However, there is little done to control spatial organization of these particles. The next section will discuss this hurdle.

1.4 Geometrical Confinement

Particles tend to collect in topological defects in a liquid crystal. In a standard nematic cell, the location of these topological defects cannot be controlled. Cells can be treated to allow preferred anchoring conditions at the edges of a cell, but the bulk cannot receive this treatment. To tackle the issue of structure self-assembly at defined locations, more defined control of liquid crystal molecule alignment is desired.

One way of overcoming this issue is with patterned substrates. Patterned substrates have shown to produce a controlled array of topological defects. Disinclination lines connect these substrates through the bulk [44]. An example of such a pattered substrate is shown in Figure 6.

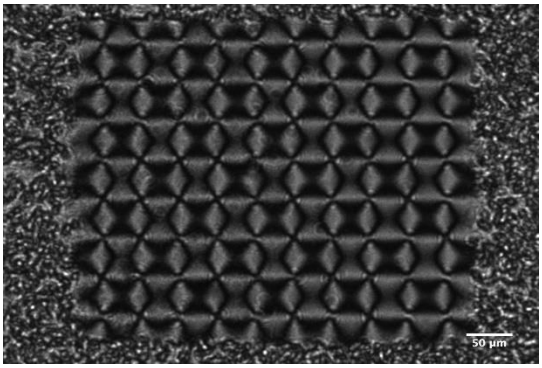

Figure 6: Patterned substrate that directs the orientation of a liquid crystal, provided by the Wei group at Kent State.

Figure 6 shows an array of topological defects where particles can gather in the nematic phase. By limiting the volume and number of locations of topological defects in the given volume, improved spatial control can be achieved. One well known liquid crystal geometry that has a limited number of defined topological defects is a liquid crystal droplet.

Liquid crystal droplets have been studied extensively, both experimentally and theoretically, and have a variety of industrial applications [50-56]. Droplets are used in polymer-dispersed liquid crystals (PDLCs). PDLCs consist of liquid crystal droplets embedded in a polymer matrix, that when subjected to an electric field [57] and have been used for privacy windows [58].

When liquid crystal droplets are suspended in solution, how the molecules at the interface interact with the solution dictate the overall molecular orientation of the droplet. Take for example the molecular structure of 5CB (Figure 3b). Both ends of the molecule are hydrophobic, so when put into water the molecules will arrange themselves with the benzine rings along the interface. This parallel anchoring condition produces what is known as a bipolar configuration. This configuration leads to two boojums, or defects, at opposite poles of the droplet. This is also true for polyvinyl alcohol aqueous solutions [59]. Putting 5CB into an aqueous solution composed of sodium dodecyl-sulfate (SDS) will result in the liquid crystal molecules aligning perpendicular to the interface, therefore a radial

configuration. SDS reduces the surface tension of the interface, allowing the molecules to exhibit a different configuration. Diagrams of these configurations are shown in Figure 7.

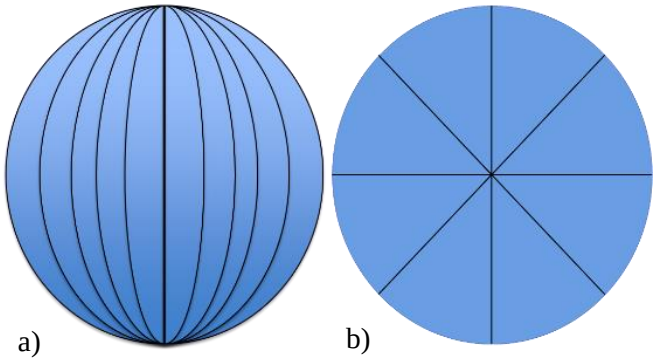

Figure 7: Diagrams of two common director configurations in a liquid crystal droplet: a) is bipolar and b) is radial.

The liquid crystal droplet has potential to provide spatial control to self-assembled structures. Due to the geometry of the droplet, topological defects form at precise locations. Taking for example the radial droplet, clusters should form at the center of the droplet when the liquid crystal goes through the isotropic-nematic phase transition. Bipolar droplets will follow suit and have clusters gather at the poles. This has already been shown with colloidal particles [60,61]. By changing concentration of quantum dots and adjusting cooling rate, more complex structures such as the hollow micro-shells can be formed at these designated locations. This is the focus of the research that will be presented.

1.5 Computational Studies of Liquid Crystals and Nanoparticles

Computational studies can help further understand these self-assembled systems. Computational studies have shown how liquid crystals orient on both flat and curved surfaces [62], how defects change and evolve on curved surfaces [63], how particles reorient themselves around molecules [61], and how liquid crystal undergoes phase transitions [64]. Both dynamic and Monte Carlo

simulations have been done, using a variety of models such as spin models and coarse-grained systems.

One important way to control nanoparticle self-assembly in liquid crystal is to control cooling rate. Understanding and controlling such parameters will allow for more control over the final self-assembled structure. Performing computations of this system will allow for easy methods of changing different parameters and seeing those effects on the system. To accomplish this, a combination of a spin-model and a dynamic phase separation model will be used. The specifics of these models will be discussed in Chapter 5.

1.6 Outline of Dissertation

Chapter 1 of this dissertation presented an outline of the research: the study of self-assembly of small nanoparticles in a liquid crystal medium. Chapter 2 will focus on the physics of the systems presented. Chapter 3 will describe liquid crystal droplet experiments with self-assembly of nanoparticle clusters and micro-shells at defined defect locations. Chapter 4 will discuss quantum dot micro-shell characterization within a liquid crystal droplet. Chapter 5 is focused on computational methods of studying nanoparticle phase separation at the isotropic to nematic phase transition point.

Chapter 2

Background and Theory

2.1 Nematic Liquid Crystal Theory - Introduction

Before we discuss self-assembly in liquid crystals, we just first set a framework for liquid crystals themselves. As stated in the introduction, nematic liquid crystals are a material that possesses orientational order and so spatial order. They can be considered as ordered fluids. A basic shape that allows for these conditions is that of a rod, which is a fine estimate for the shape of 5CB (see figure 3b). To develop a successful theory of liquid crystals, we must note parameters that are seen in experiments.

Experiments show us that nematic liquid crystals are spatially non-polar. That is there is no defined difference if a molecule is pointed in the +x direction or -x direction. Since there is no defined spatial polarity, liquid crystals have their spatial directions characterized by an order parameter. This order parameter is a scalar number that relates the directions of the liquid molecules to a preferred direction. Liquid crystals also experience diverse types of deformation, so we need a way of characterizing these deformations. Finally, liquid crystals are very sensitive to temperature, i.e. liquid crystal molecules are subject to fluctuations from energy on the order of kT. A thorough understanding of all these factors is necessary before discussing self-assembly of particles in a liquid crystal in Chapter 3.

2.1.1 Nematic Orientational Order

Nematic orientation is characterized by a scalar order parameter. As stated in Chapter 1, nematic liquid crystals tend to align in a general direction which is labeled by a vector we call the director. The nematic order parameter is a measure of how aligned liquid crystal molecules are aligned with the director. Nematic

molecules do not fully line up with the director due to thermal fluctuations [65], so the scalar order parameter is a way of accounting for those thermal fluctuations.

The scalar order parameter is defined as

$$S = < P_2(\cos\theta) > \quad (1)$$

where θ is the angle between the long molecular axis and the director (Figure 8) and is averaged over a set of N molecules. The second order Legendre polynomial ensures the scalar order parameter doesn't depend on the polar direction of the molecule. It also ensures that the range of the order parameter is $0 \leq S \leq 1$. If S = 0, the liquid crystal is in the isotropic phase. There is no directional order in the isotropic phase. If S = 1, the molecules are perfectly aligned. Nematic values of S range from 0.3 to 0.8 [66].

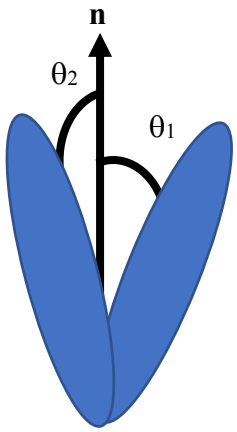

Figure 8: Schematic of nematic molecule lining up with the nematic director.

The scalar order parameter can also be linked directly to the director itself. A tensor can be constructed of the form [66]

$$Q_{a,b} = S(n^a n^b - \frac{1}{3}\delta_{ab}) \quad (2)$$

known as the Q-tensor. Here, n^a and n^b represent the x, y, or z components of the director, and $\delta_{ab}$is the Kronecker delta. In three dimensions, the Q-tensor is written as

$$Q = S\begin{bmatrix} Q_{xx} & Q_{xy} & Q_{xz} \\ Q_{yx} & Q_{yy} & Q_{yz} \\ Q_{zx} & Q_{zy} & Q_{zz} \end{bmatrix} \tag{3}$$

This tensor is symmetric and traceless, since by Equation 2, Q_{xy}= Q_{yx} (true for x, y, and z), and $Q_{zz} = -(Q_{xx} + Q_{yy})$. Q is a tensor with five degrees of freedom. Equation 3 can be diagonalized to find the eigenvectors of the matrix. After diagonalization, we get

$$Q = \begin{bmatrix} \frac{2}{3}S & 0 & 0 \\ 0 & -\frac{S}{3} & 0 \\ 0 & 0 & -\frac{S}{3} \end{bmatrix} \tag{4}$$

From Equation 4 we can obtain the eigenvalues and corresponding eigenvectors. For the Q-tensor, the largest eigenvalue obtained is the order parameter, and the corresponding eigenvector is the director.

2.1.2 Phase Transitions

Liquid crystals whose phases change with changing temperature are called thermotropic. The nematic liquid crystal 5CB is one such material. So as 5CB goes from isotropic to nematic, what kind of phase transition is this? For nematic liquid crystals, this is specifically a first order phase transition. In thermodynamics, this is represented as a discontinuity in the entropy as you change temperature at constant volume [66]:

$$\boldsymbol{S} = -\frac{\partial F}{\partial T}\Big)_V \tag{5}$$

Here, F is the free energy of the system. The scalar order parameter of a nematic liquid crystal also experiences a discontinuity at the temperature of the isotropic-nematic phase transition. To study this we must examine the Landau formalism of phase transitions.

The Landau formalism of phase change can be written in terms of the Q tensor. This free energy density is

$$f(Q) = \frac{A}{2}(T - T_{NI})trQ^2 + \frac{B}{3}trQ^3 + \frac{C}{4}trQ^4 \tag{6}$$

where T_{NI} is the isotropic-nematic temperature, and A, B, and C are material constants. Typical values for these constants are A = 10^5 J/mK, B = -10^6 J/m, and C = 10^6 J/m [65]. Note there is no trQ term due to Q being a traceless tensor. Looking back at Equation 4, it is easy to show that $trQ^2 = 2S^2/3$. With this we can rewrite Equation 6 in terms of the order parameter:

$$f(S) = \frac{a}{2}S^2 + \frac{b}{3}S^3 + \frac{c}{4}S^4 \tag{7}$$

Note that the constant a is proportional to the temperature difference in Equation 6. We can treat a as our effective temperature.

We are now ready to verify that the nematic liquid crystal exhibits a first order phase transition. On one side of the phase transition, we expect the liquid crystal to be stable in the isotropic phase. On the other side, we expect a stability in the nematic phase. This tells us that $f(S)$ will have varying minima depending on the value of a (i.e. temperature). Figure 9 shows plots of $f(S)$ vs S for varying

values of *a*. In Figure 9a we see that there is only one minimum for f(S): S = 0. This indicates that at this temperature, we are in the isotropic phase. Figure 9b shows the formation of a second minimum as we decrease temperature. Figure 9c shows the existence of a meta-stable state of both isotropic and nematic regimes. Finally Figure 9d shows a new global minimum at S = 2/3: the nematic phase.

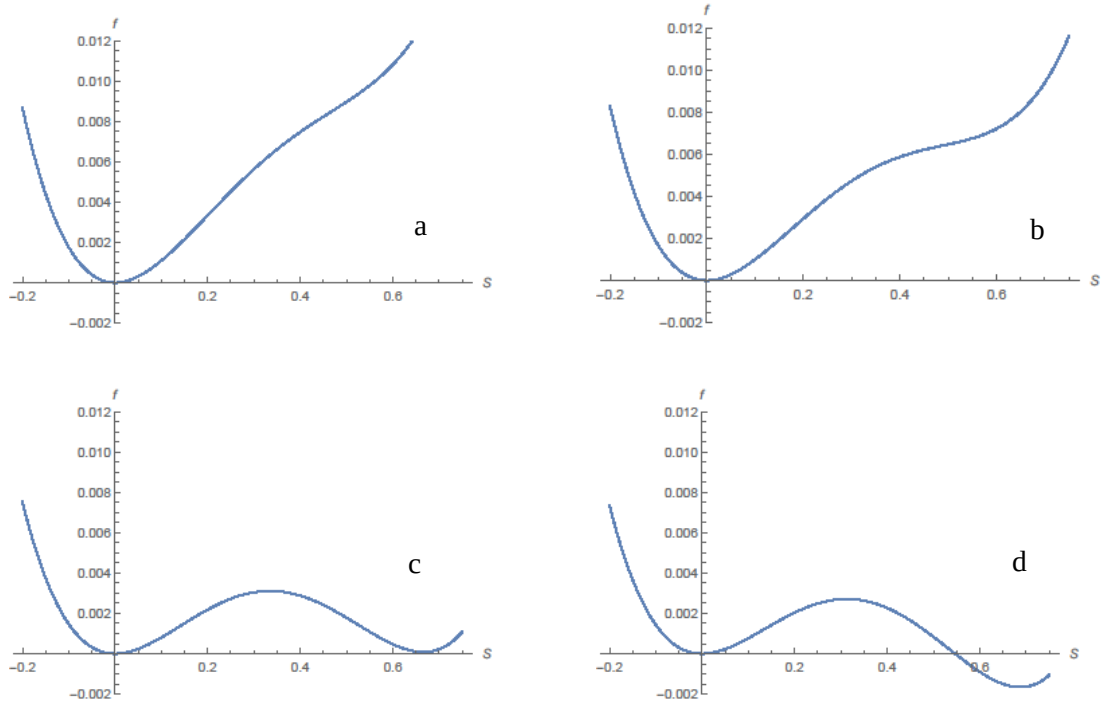

Figure 9: Plots of the Landau energy as a function of different temperatures. a) exhibits a single minimum as S=0 (isotropic phase). b) shows the development of a second minimum (possible isotropic phase). c) shows two minima for both isotropic and nematic states. d) shows the new minima in the nematic phase.

To see the first order phase transition, we minimize Equation 7 and solve for the critical points. Those critical points are

$$S = 0, \frac{-b \pm \sqrt{b^2 - 4ac}}{2c} \tag{8}$$

By plotting the second critical point vs changing values of *a* we obtain Figure 10.

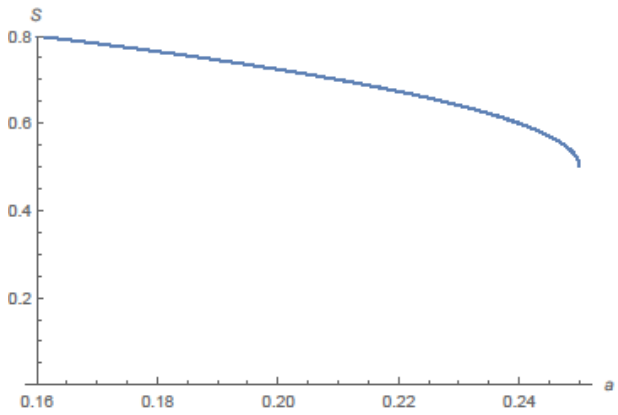

Figure 10: Plot of the nematic order parameter as a function of effective temperature. At a specific temperature (a = 0.25) there exists a discontinuity in the order parameter, showing a first-order phase transition.

Figure 10 shows the discontinuity in S. We can then conclude that the isotropic-nematic phase transition is first order. We see this same symmetry-breaking in classic spin models in studying magnetization, such as the Ising model [67].

This concludes a brief study of the Landau energy regarding nematic liquid crystals. We have shown that there exists a first-order phase transition. This is not the only energy involved however. As stated in Chapter 1, there are elastic deformations and orientational frustrations in a liquid crystal. This elastic energy is the topic of the next section.

2.1.3 Elastic Energy in a Liquid Crystal

Nematic liquid crystals can experience several different elastic deformations. These are most commonly known as splay, twist, and bend (See Figure 11). Splay occurs when molecular orientation is perpendicular to a gradient

direction (Figure 11a). Twist occurs when molecular orientation changes as you travel through different planes (Figure 11b). And bend occurs when molecular orientation is parallel to a gradient direction (Figure 11c).

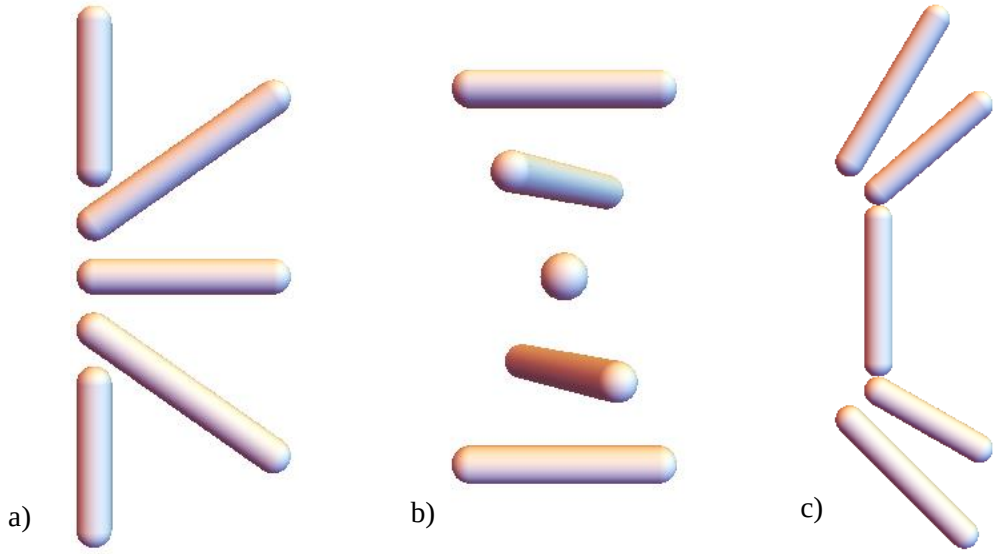

Figure 11: Schematic of different deformation of a nematic liquid crystal: a) splay, b) twist, and c) bend.

The free energy density of these deformations is written as

$$f_{el} = \frac{K_1}{2}(\nabla \cdot \vec{n})^2 + \frac{K_2}{2}(\vec{n} \cdot \nabla \times \vec{n})^2 + \frac{K_3}{2}(\vec{n} \times \nabla \times \vec{n})^2 \quad (9)$$

In this equation, K_1, K_2, and K_3 are the elastic constants for splay, twist, and bend respectfully. This is known as the Frank free energy.

We now have two types of energy that govern liquid crystal dynamics: elastic and phase-transitions. We can add these two energies together and obtain the known Landau de Gennes energy

$$F_{LdG} = f_{el} + f \tag{10}$$

We now have an interesting question to solve regarding this energy. Given a certain geometry, how will the liquid crystal orient itself to minimize its energy? We begin this problem by working in a 2D system for easier calculations. Regarding Equation 9, the elastic constants in practice are not identical. They are, however, within the same magnitude of each other. To make calculations easier, we can assume a one-constant approximation of the Landau de Gennes free energy. By setting the elastic constants equal, Equation 10 becomes

$$F_{LdG} = f + \frac{K}{2}((\nabla \cdot \vec{n})^2 + (\nabla \times \vec{n})^2) \tag{11}$$

This is known as the one constant approximation. While at most times easier to work with, for our purposes we will use Equation 9 for now and return to Equation 11 later. The one constant approximation will be used in Chapter 5 for computational purposes.

We first parameterize the director $\vec{n}$ with the form $\vec{n} = \cos\theta\, \boldsymbol{x} + \sin\theta\, \boldsymbol{y}$. We now seek to solve for the configuration the director will take to minimize Equation 9. We begin by defining two new constants: $J = \frac{K_1+K_3}{2}$ and $D = \frac{K_1-K_3}{2}$. Deem was the first to propose this method for calculations [68]. We then rewrite Equation 9 as

$$f_{el} = \frac{1}{2}((J+D)(\nabla \cdot \vec{n})^2 + (J-D)(\vec{n} \times \nabla \times \vec{n})^2) \tag{12}$$

After inserting the parameterization of the director into Equation 12 and using the Euler-Lagrange equations to minimize, we obtain

$$-J\left(\theta_{xx}+\theta_{yy}\right)+D\left(\theta_y^2-\theta_x^2+2\theta_{xy}\right)\sin 2\theta+D\left(\theta_{xx}-\theta_{yy}+2\theta_x\theta_y\right)\cos 2\theta=0 \quad (13)$$

The solution to Equation 13 is θ equals a constant. This implies that all the molecules of a nematic liquid crystal lie along the same director. This is reasonable: no deformation implies the lowest free energy state. There are, however, more solutions to discuss. We begin by changing the parameterization of the director from cartesian to polar. We can rewrite the director as $\vec{n}=\cos\varphi\,\boldsymbol{r}+\sin\varphi\,\boldsymbol{\theta}$. Once again, we insert the director into Equation 12 and after minimization, and some algebra, we obtain

$$-(J-D\cos 2\varphi)\left(\varphi_{rr}+\frac{\varphi_r}{r}\right)-D\left(\varphi_r^2+\frac{1}{r^2}\right)\sin 2\varphi=0 \quad (14)$$

The solutions to this equation are $\varphi=0,\ \frac{\pi}{2}$. Inserting these possible values into the director we obtain our other possible director configurations. Figure 12 shows the following director plots.

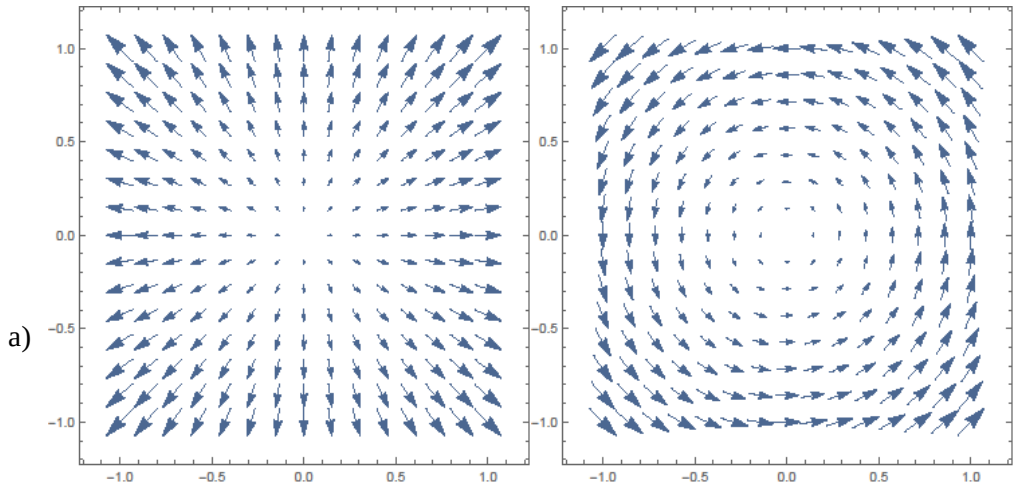

Figure 12: Two diagrams of defects in a polar phase. a) shows a splay defect and b) shows a bend defect.

Interesting behavior arises if we allow the director to rotate in the plane (the benefit of using polar coordinates). Figure 12a shows a splay pattern. Figure 12b shows a spiral pattern. These correspond to the possible deformations allowed in the elastic free energy: splay or bend. What is of interest is what is at the center of these plots. The directionality of the director becomes difficult to make out. We can say that there exists some frustration in the director. This is what's known as the topological defect.

2.1.4 Topological Defects

Topological defects are areas of orientational frustration in a liquid crystal. They can occur spontaneously in a bulk nematic as the phase transition occurs, or because of surface treatment or geometric restriction [43]. We will now discuss how we label topological defects and distinguish between them.

To distinguish different topological defects, we use the Burgers circuit [65]. We will impose a circuit around a topological defect in Figure 13.

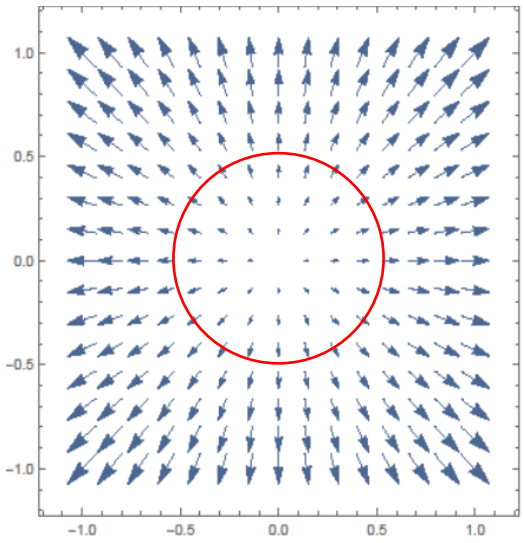

Figure 13: Burgers circuit around a defect point. The circuit is followed around in the counter-clockwise direction.

We can identify the type of defect present by giving the defect a topological charge. To obtain this charge, we follow the circuit around the counter-clockwise direction and see how the director rotates while following the path. In Figure 13, beginning on the right side of the circuit, we see the director rotates north, west, south, and back to east. The director makes one full rotation as we follow the circuit, so we label this defect as having a +1 charge. We can write this mathematically as

$$\oint d\varphi = 2\pi q \tag{15}$$

where q is the topological charge. There are various possible defect charges, and those are highlighted in Figure 14.

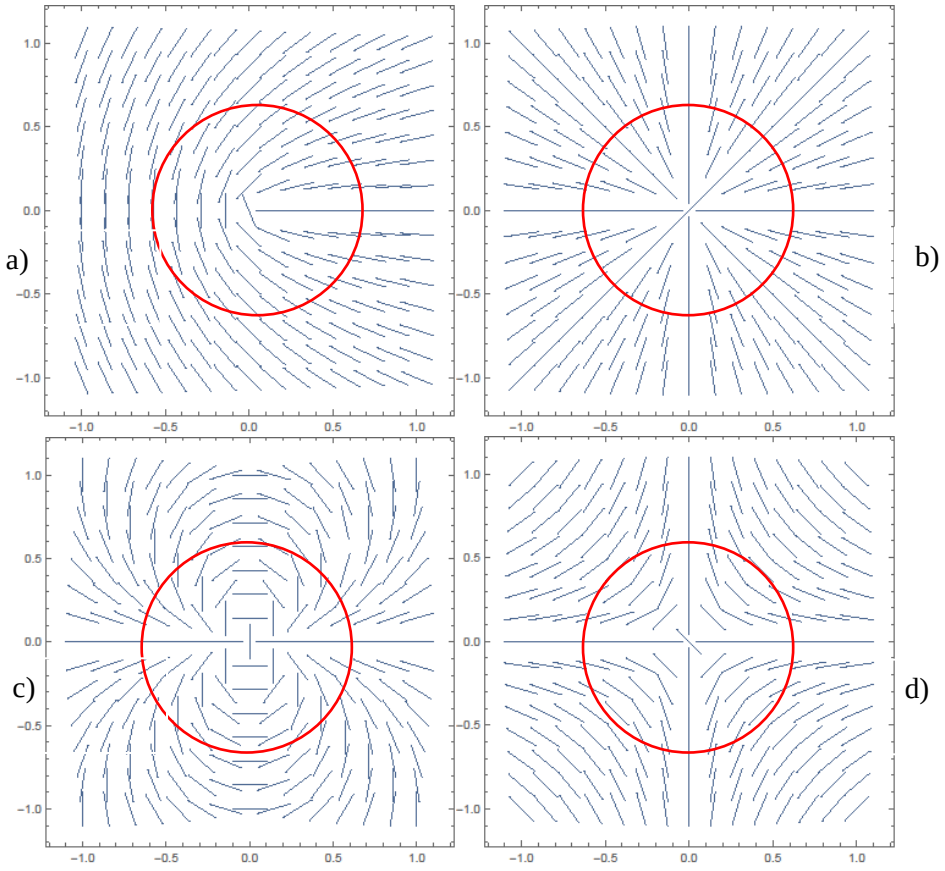

Figure 14: Various nematic defect configuration. a) is the +1/2 defect, b) is the +1 defect, c) is the +2 defect, and d) is a -1 defect.

We can obtain director configurations that describe all these possible defects. We begin once again with the polar parameterization of the director: $\vec{n} = \cos\varphi\, \boldsymbol{r} + \sin\varphi\, \boldsymbol{\theta}$. Inserting this director into Equation 11 we get

$$F_{LdG} = f + \frac{K}{2}(\nabla\varphi)^2 \tag{16}$$

Minimizing this equation, we obtain

$$K\nabla^2\varphi = 0 \tag{17}$$

whose solution is

$$\varphi = \varphi_0 + q\theta \tag{18}$$

where q is once again the charge of the defect. So, with any charge q we can determine the director configuration of any defect, as plotted in Figure 14. We can now take this director orientation and calculate free energies of defects. We will insert Equation 18 into Equation 16 and integrate (negating the Landau energy since it is simply a constant in this case):

$$F = \int_a^R \int_0^{2\pi} \frac{K}{2}\left(\frac{q}{r}\right)^2 dr d\theta \tag{19}$$

$$F = \pi K q^2 \ln\frac{R}{r_c} \tag{20}$$

The limits of r are chosen to prevent a divergence in the calculations. R is the max distance away from the defect (usually sample size) and r_c is the minimum distance away from the defect core. The Frank free energy is not valid at small distances due to the $1/r$ dependence, so a constant is usually added to the defect free energy to account for the energy of the defect core. The term of interest in the free energy of defects is the q^2 term.

In a 2D nematic liquid crystal, or a 3D shell of nematic liquid crystal, +1 defects are not observed. In place of a singular +1 defect are two +1/2 defects [69]. A simple energy analysis confirms this. In Equation 20, if we let q = 1, we get $F = \pi K \ln\frac{R}{a}$. Now if we let q = 1/2 and account for two of these defects, we get $F = \frac{1}{2}\pi K \ln\frac{R}{a}$. In nematic liquid crystals, it is energetically more favorable to adopt two +1/2 defects than a singular +1 defect.

2.1.5 Simulations of Topological Defects

Simulations provide an excellent tool of studying physical phenomena while being able to change different experimental parameters without the need of expensive lab work. In this section we will discuss the simulation of topological defects and their relation to bulk systems, specifically curved systems. This work will be related to the study of liquid crystal droplets in Chapter 3.

Spin model systems are ideal for studying liquid crystals, as spin models exhibit several similar behaviors as liquid crystals, such as phase transitions and the production of topological defects. Two spin models that will be discussed here are the XY model and the Lebwohl-Lasher (LL) model [62, 70]. In both models, spins interact with their neighbors via a given energy. For the XY model, the energy is given as

$$H = -J \sum_{<i,j>} \vec{s_i} \cdot \vec{s_j} \tag{21}$$

where the sum is over nearest neighbors. The LL model is a similar energy given by

$$H = -\epsilon \sum_{<i,j>} (\vec{s_i} \cdot \vec{s_j})^2 \tag{22}$$

J and ε are interaction energies between the spins. The squared dot product ensures the condition of $\vec{n} = -\vec{n}$, which is that in nematics there is no energetic difference in the head of the molecule pointing in one direction or the opposite. These energies will be used on a system of spins using a Monte Carlo method of annealing. This is done to visualize the different topological defects that will occur.

The Monte Carlo method used is an annealing process to achieve a ground state configuration. In Monte Carlo, random numbers are generated to change some parameters of what is being simulated. In this case, the spin's directions are randomly adjusted by a set amount. At the beginning of the simulation, a random spin is chosen. That spin's energy is calculated via either Equation 21 or 22. That spin's direction is then adjusted, and a new energy is calculated. If the new energy is lower than the old energy, the new configuration is accepted. If the new energy is higher, the new configuration is accepted based on some probability $e^{-\Delta E/kT}$. This is done to allow the system to escape some undesired metastable state. Once the configuration has been decided, a new spin is chosen at random. This is repeated until all spins have been explored. After this point, the value to kT is lowered and the process repeats again until the final temperature is reached.

Spin model systems can also be moved forward in time dynamically using the following equation:

$$\frac{\partial \theta}{\partial t} = -\frac{\partial H}{\partial \theta} + \gamma \tag{23}$$

The spins are moved forward in time in steps that decrease the overall free energy of the system. In this equation θ is the angel the spin makes with the positive x-axis. The γ term is added as a fluctuation to the spin: it acts as the temperature bath. This is the Langevin heat bath which has the form

$$\sqrt{\frac{2\pi kTdt}{g}}\vec{\tau} \tag{24}$$

where g is the drag coefficient, dt is the timestep of the evolution, kT is the temperature, and $\vec{\tau}$ is a random number generated from a normal distribution with a mean of 0 and variance of 1.

To visualize the final state, simulated crossed polarizers are used. When visualizing liquid crystals under a microscope, crossed polarizers are used to determine molecular orientation and to identify defects. The orientation of liquid crystal molecules rotates the polarization of incoming light due to the optical anisotropy of the material. By viewing through crossed polarizers, the portion of light that is rotated makes it to the eye piece, allowing for the orientation to be determined. Liquid crystal molecules that are aligned at 0° or 90° will appear dark between crossed polarizers. This means that the intensity of the light seen should have a maximum between 0 and π/2 radians. The intensity of light seen from liquid crystals is given by [28]

$$I = I_0(\sin 2\theta)^2 \tag{25}$$

Figure 15 shows the intensity pattern following this formalism.

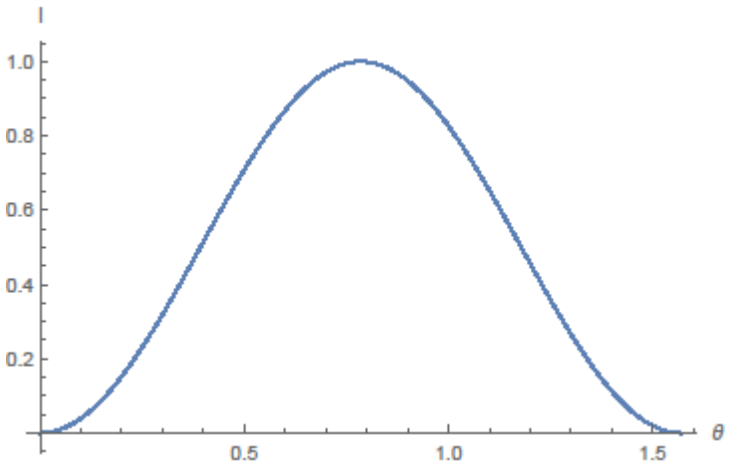

Figure 15: Plot of intensity of light given by Equation 25. Peak intensity is reached at $\pi/4$ radians.

We can now visualize the XY and LL models as if they were seen through crossed polarizers. Figure 15a shows the simulated cross-polarized image of the XY model. Note that each defect point has 4 black brushes. This is the sign of a +1 defect at that location. Figure 15b shows a similar crossed polarized image, however there are only two brushes appearing from the defect locations. This is the sign of a +1/2 defect. These visualizations aid us in determining uses for these models.

The XY model is a polar system, represented as spins with an arrow head. Systems that exhibit this behavior are smectic liquid crystal phases and lipid bilayers. The LL model is a non-polar system: these spins do not have an arrow head. This makes the system a good model for a nematic liquid crystal. These spin models also exhibit phase transitions. Figure 17 is a plot of the average energy per spin in the LL model as a function of temperature. Equation 22 is simply averaged over the entire system of N spins. As a specific temperature, there is a significant increase in energy, signifying a phase change like that of a liquid crystal.

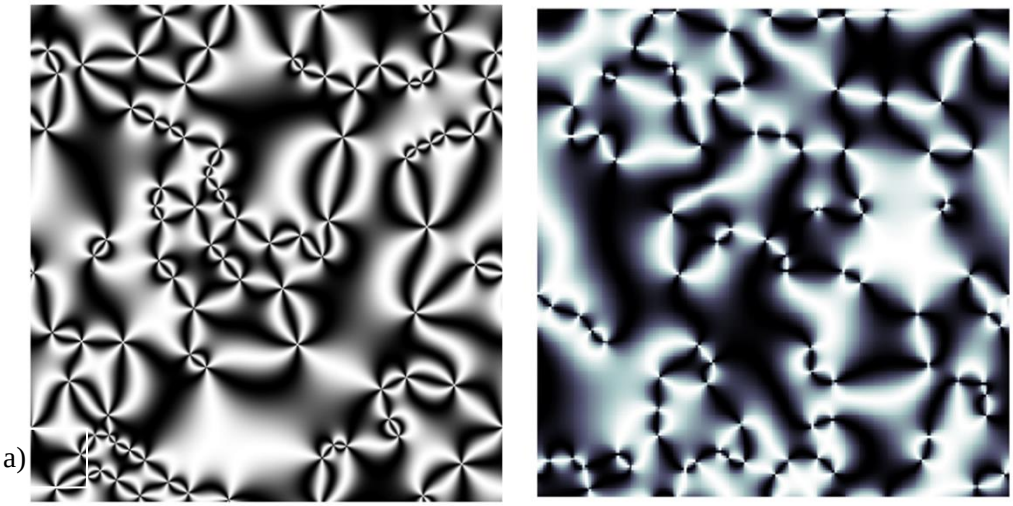

Figure 16: Simulated crossed-polarized images of liquid crystals with a) +1 defects and b) +1/2 defects.

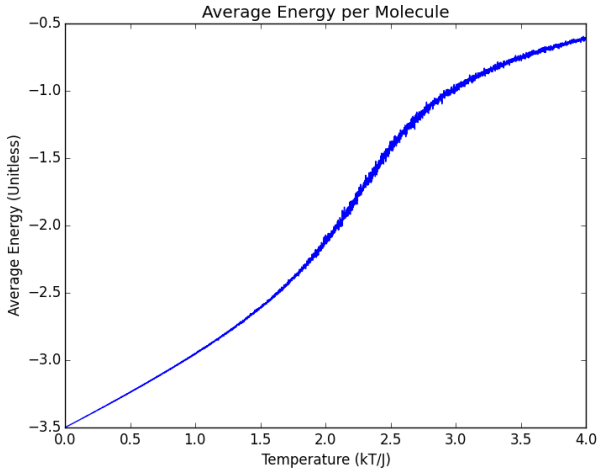

Figure 17: Plot of average energy per spin of the Lebwoho-Lasher model as a function of temperature. The jump in energy indicates a phase change.

2.1.6 Topological Defects in Liquid Crystal Droplets

Confining liquid crystal to certain geometrical shapes allows control over where the topological defects occur. This section presents the geometrical shape

of choice for this dissertation's focus: the sphere. By restricting liquid crystal to a sphere, we obtain a liquid crystal droplet.

The interface between a liquid crystal droplet and the droplet's solution governs the molecular orientation of the liquid crystal molecules within the droplet. This occurs due to the interface setting the boundary conditions of the droplet. If the molecules are oriented perpendicular to the surface of the droplet (homeotropic alignment) the droplet exhibits a radial configuration. This results in a hedgehog defect at the center of the droplet. If the molecules are aligned parallel at the interface of the droplet, a bipolar configuration is obtained with two defects located at opposite poles of the droplet. This follows the Gauss-Bonnett theorem of topology relating total topological charge to the shape of the geometry [62]. Director configurations of both radial and bipolar orientations are presented in Figure 18.

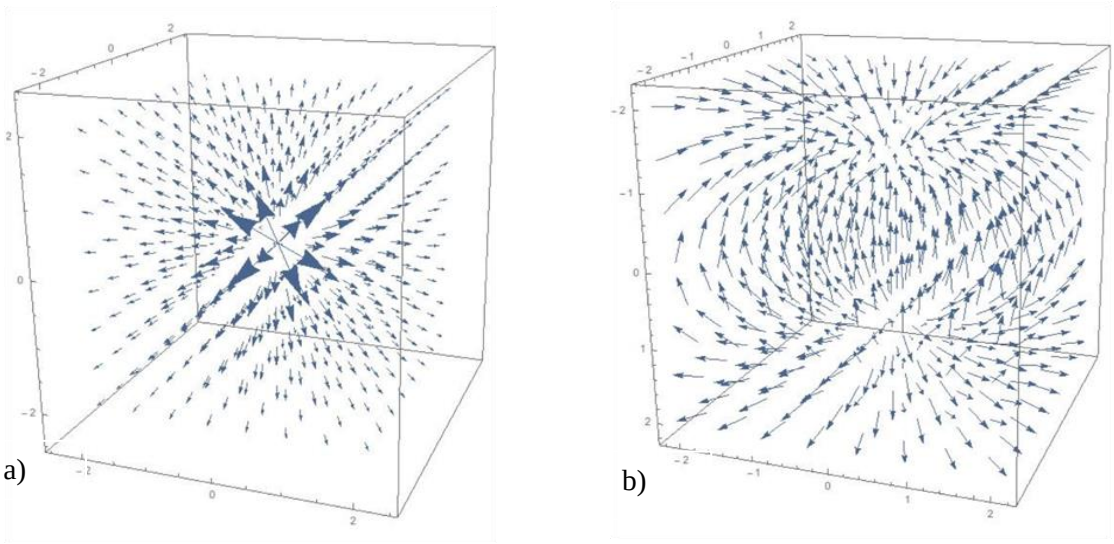

Figure 18: Director configurations for both a) radial and b) bipolar liquid crystal droplets.

The free energies of these configurations are easy to calculate as well. Using Equation 11, the one constant approximation of the Frank free energy, and

integrating the free energy density over a droplet of radius R, we obtain their corresponding free energies:

$$F_r = 8\pi KR \tag{26a}$$

$$F_B = (\frac{11}{2} - G)\pi KR \tag{26b}$$

G is known as Catalan's constant is approximately 0.916.

This concludes discussion on the physics of liquid crystals. There are much more interesting topics in this field that could be covered, however, the topics chosen are limited to those directly related to the work presented in this dissertation. The following sections discuss the insertion of nanoparticles into a liquid medium, so Brownian motion will be discussed. The following section will cover the particles of interest themselves: quantum dots.

2.2 Quantum Dots in a Fluid

When particles are inserted into a liquid crystal, the phase of the material will govern the motion that particles experience. Initially in the experiments presented, particles are inserted into the isotropic phase of the liquid crystal. While in this isotropic fluid, particles will exhibit Brownian motion. Particles tend to dislike a liquid crystal medium. Even after long mixing times, particles tend to stay clustered together [43]. Recent research has shown that by functionalizing particles with mesogenic ligands, uniform dispersion is achieved, and particles behave as in a standard fluid. In the following section Brownian motion will be discussed, followed by how particles behave once the liquid crystal goes from the isotropic phase to the nematic phase. The particles of interest are quantum dots.

2.2.1 Brownian Motion in an Isotropic Fluid

Brownian motion occurs when a particle collides with the molecules composing the surrounding solvent. All these collisions cause the particle to follow a random path through the fluid. The total distance traveled through the fluid in a given time is dependent on several parameters such as temperature, particle size, and fluid viscosity. Brownian particles experience diffusion through the fluid as they move in random paths through the fluid and spread out from one another. We can then say that the density of particles in a fluid should satisfy the diffusion equation, given by

$$\frac{\partial \rho}{\partial t} = D \frac{\partial^2 \rho}{\partial^2 x} \tag{27}$$

The solution to this equation is given by

$$\rho(x,t) = \frac{1}{\sqrt{2\pi\sigma^2}} e^{-x^2/4\sigma^2} \tag{28a}$$

$$\sigma^2 = 2dDt \tag{28b}$$

where d is the dimension of the diffusion problem (1,2, or 3), D is the diffusion constant, and t is the time of diffusion. Equation 28a is plotted in Figure 19 at various times to show the density of particles spreading out.

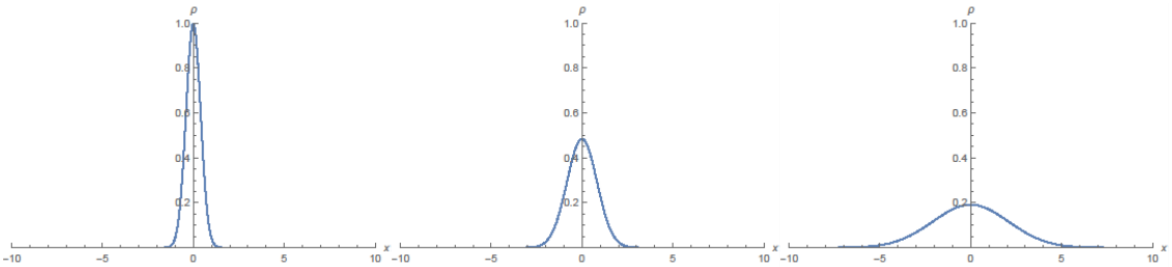

Figure 19: Plots of the solution of the diffusion equation (26a) with d = 2, D = ¼, with increasing values of t from left to right.

The diffusion constant in a isotropic medium, D, can be easily calculated by the Einstein-Stokes relation:

$$D = \frac{kT}{6\pi\mu r} \tag{29}$$

Here, r is the radius of the particle, and μ is the viscosity of the surrounding fluid. It is interesting to note how these diffusive properties appear from random motions of these particles. We can also examine the motion of these particles explicitly and obtain a way of measuring diffusivity. Figure 20a is a plot of the trajectories of 10 random walkers making 20 random steps. Measuring the mean distance traveled would result in an average of zero due to the random steps taken. If we examine the second moment of the motion (the mean-square displacement) we see a linear behavior in time. The slope of this line is proportional to the diffusivity of the system. The plot of mean-square displacement vs steps taken (i.e. the time) is shown in Figure 20b.

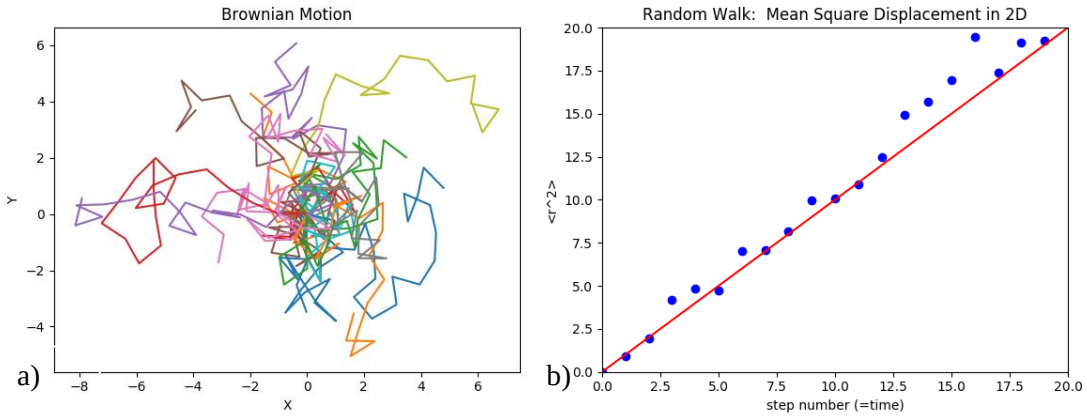

Figure 20: a) Plot of the Brownian motion of 10 walkers making 20 steps. b) Plot of the means square displacement vs time of the walkers in a).

2.2.2 Driven Motion in a Nematic Fluid

Particles in a nematic fluid will not be driven simply by Brownian motion. As a liquid crystal goes from the isotropic phase to the nematic phase, the viscosity will increase as well. By Equation 29, this will decrease the diffusivity of the particles in the fluid. In the case of a nematic liquid crystal, elastic properties develop as well with the increased viscosity. The elastic behavior acts to oppose deformation of the liquid crystal director.

As the isotropic-nematic phase transition occurs, particles will be expelled out of the growing nematic domains and collect in the shrinking isotropic regimes. This avoids any unnecessary elastic deformation in the nematic phase and allows the particles to explore the isotropic regions. As the isotropic domains continue to shrink, particles will begin to aggregate together and cluster. This results in a phase-templated clusters that are scattered in the nematic phase, with topological defects surrounding the clusters [46].

Another way of lowering the free energy of the liquid crystal with particles inserted is to have the particles gather directly at topological defects. Instead of

creating new topological defects at the location of inserted particles, nematic forces drive the particles to already existing areas of high energy. This has been verified both experimentally and computationally [61]. This holds for both micron-sized particles and nanoparticles (~10 nm diameter).

2.2.3 Quantum Dots

Quantum dots are nano-sized semiconductor particles whose photonic properties are governed by their size. When quantum dots of a specific size are excited by light of a certain wavelength, the photons are absorbed, and photons of longer wavelengths are emitted. This occurs due to the electrons absorbing enough energy to jump across the band-gap of the quantum dots. The amount of energy released by the quantum dot is described by a sum of the band-gap energy and the energy of confinement. This is known as the Brus equation [71] and is given by

$$\Delta E = E_{gap} + \frac{h^2}{8r^2}\left(\frac{1}{m_e} + \frac{1}{m_h}\right) \tag{30}$$

where h is Planck's constant, r is the radius of the quantum dot, m_e is the effective mass of the electron, m_h is the mass of the hole when the electron crosses the band-gap, and r is the radius of the quantum dot. Using the Brus equation, we can relate this energy to the wavelength of light emitted by $E = {}^{hc}/_{\lambda}$. The relation between wavelength and quantum dot radius is shown in Figure 21. From this it follows that larger quantum dots will emit at higher wavelengths of light when excited.

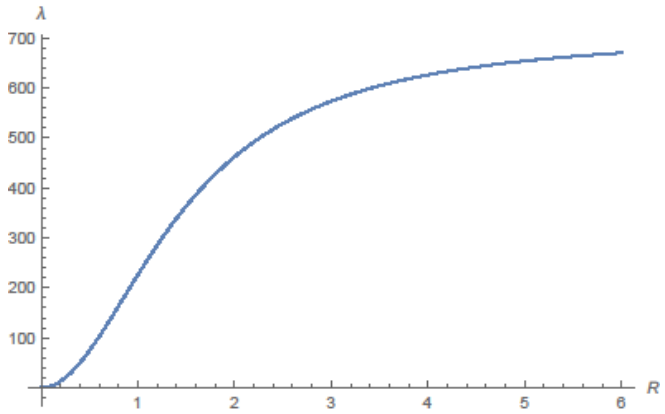

Figure 21: Plot of the wavelength of light emitted by an excited quantum dot in nm vs quantum dot radius in nm.

The emissive properties of quantum dots make them ideal for studying self-assembly in liquid crystals. Being able to easily visualize the quantum dots as they are subject to elastic forces during the isotropic-nematic phase transition allows for easy visualization of the self-assembly mechanics and phase behavior. As the self-assembly process is further understood, other particles can be substituted for different applications.

2.3 Conclusions

The theory behind the topics covered in this dissertation have been presented. Elastic properties of nematic liquid crystals and the production of topological defects provide a method to study self-assembly of functionalized quantum dos in liquid crystal. The properties of quantum dots allow for visualization of particle motion during phase changes which in turn allows for the visualization of phase change mechanics due to quantum dot motion. Topological defects are areas of high energy in a liquid crystal which provide locations for quantum dots to gather to limit the amount of elastic deformation experienced by liquid crystal molecules and to reduce the free energy of the system. These factors will be the focus for understanding the experiments conducted in the following chapters.

Chapter 3

Quantum Dot Self-Assembly in Liquid Crystal Droplets

3.1 Introduction

Liquid crystals have shown to provide a viable medium to allow the self-assembly of nanoparticles. More specifically, the topological defects present in a liquid crystal are known to drive this self-assembly due to the elastic interactions in the medium. Micron sized particles can be arranged at topological defects to create lattice-like structures [60]. Several types of structures have been formed utilizing topological defects in liquid crystal, using particles that range from nano- and micro-sized particles, as well as biological materials.

Self-assembly of nano-sized particles (~10 nm diameter) proves to be more of a difficult challenge, as particles of that size range are subject to strong Brownian fluctuations. Utilizing a liquid crystal medium to aid in the self-assembly process helps to alleviate this issue. The energy scale of the Brownian fluctuations is on the order of kT. As these fluctuations become comparable to the free energy cost of inserting a particle into a liquid crystal host, spontaneous assembly mediated by the Frank elastic energy occurs. Dispersed particles in the liquid crystal explore the anisotropic fluid thermally and assemble at free energy minima by clustering together and/or locating at topological defect cores.

Several attempts have been made to self-assemble various types of nanoparticles in a liquid crystal, such as quantum dots, metallic particles (gold, silver) and magnetic particles [48, 72]. These self-assembled structures may exhibit collective electronic, photonic, or magnetic properties not seen in single nanoparticles. Typically, particle clustering results in isolated aggregates, or clusters, with no internal ordering of the particles or positional control. An alternative to this is to functionalize the nanoparticles with a carefully designed ligand, which results in fascinating 2D structures of particles [47].

This Chapter focuses on work proposed to control the spatial organization of nanoparticle clusters and other assemblies. The approach is to use liquid crystal droplets in the nematic phase to control the positioning and size of clusters. Micron-scale droplets should be easy to manipulate by external methods (optical trapping, surface patterning, electric fields, etc).

The nematic liquid crystal phase is a phase composed of an anisotropic fluid and is characterized by orientational order defined locally by the director. Orientational frustration can occur and produce topological defects. For example, the homeotropic anchoring conditions in a liquid crystal droplet (radial configuration, Figure 18a) results in a single hedgehog defect located at the droplet center.

Previous work has shown that inserted nanoparticles into a nematic liquid crystal results in pinning to surface defects in liquid crystal droplets [61]. Our work takes a different approach. Initially the particles are dispersed into isotropic droplets, and then subsequently cooled to the nematic phase. This approach is partially motivated by the inherent difficulties in manipulating single nanoparticles. It also allows the observation of cluster formation free from outside manipulation.

Small particles are chosen to allow for spontaneous self-assembly without the influence of any external forces. These particles are very mobile due to Brownian fluctuations and locate at defect points. 6 nm quantum dots exhibit these behaviors and are also used for their emission properties.

While self-assembly via topological defect locations is an effective strategy, recently another mechanism for spatial nanoparticle sorting in liquid crystal was developed [46]. Results demonstrated that the moving isotropic to nematic phase front can act as an elastic sorting mechanism for the nanoparticles. Of particular interest is the formation of stable micro-shells. These structures were formed using quantum dots with mesogenic ligands [47] providing an added degree of control in particle dispersion and cluster stabilization. While closely packed, the mesogenic ligands provide a short-range attractive interaction between nanoparticles.

In this Chapter two assembly mechanisms in liquid crystal droplets with different surface anchoring conditions (planar and homeotropic) are investigated. These two mechanisms are titled "equilibrium defect sorting" and "phase transition sorting". By varying droplet cooling rate through the isotropic-nematic phase transition, different particle distributions in the liquid crystal droplets induced by defect locations and particle assembly at energetically unfavorable locations are observed. It is also observed that single quantum dot micro-shells can be formed at the center of liquid crystal droplets.

Understanding the competition between defect-based assembly and phase-transition-induced assembly is important for controlling the position of nanoparticle clusters over large length-scales without the need of outside influences. Clusters isolated in liquid crystal droplets are also observed to be close-packed and produce macroscopic assemblies of nanoparticles in two and three dimensions.

3.2 Materials and Methods

Quantum dots were functionalized with a mesogenic ligand. This ligand is of the type investigated by Dunmur [73] and Vashchenko [74]. It was prepared following the sequence of reactions reported in [47], and then exchanged with octadecylamine surface ligands on commercial CdSe core/ZnS shell quantum dots (NN Lab Inc., Fayetteville, AR, USA) following reported procedure [48]. This ligand stabilizes particle clusters via short range non-covalent interactions, which facilitates particle dispersion in the host liquid crystal matrix (4-cyano-4'-pentylbiphenyl, 5CB) and produces a uniform dispersion of modified quantum dots in the isotropic phase [46]. In addition, above a certain threshold concentration, the ligand allows for unique micron-scale capsules [47] by a unique phase separation process.

The modified quantum dots are uniformly dispersed in isotropic 5CB via heat bath sonication at 50 °C for 2 hours, verified by fluorescent microscopy. Particle concentrations used in these experiments varied from 0.05 to 0.2 wt %.

After sonication, droplets were formed. 3 mL of the quantum dot – 5CB composite was pipetted into 300 mL of either Millipure water or 1.0 wt% polyvinyl alcohol (PVA) / water solution at a temperature of 55 °C. 5CB droplets in our water typically exhibit homeotropic boundary conditions resulting in a radial configuration which was verified by cross-polarized microscopy, whereas droplets in PVA/water exhibited planar boundary conditions resulting a bipolar configuration. To follow standard practice for creating nematic droplets, 5CB was dispersed in 1.0 wt% sodium dodecyl sulfate (SDS) to achieve homeotropic boundary conditions, and pure glycerol to produce planar boundary conditions. After adding the quantum dot – 5CB composite to the aqueous solution, the system was then tip sonicated using a cell disrupter for approximately one second, until the resulting emulsion appeared cloudy, keeping the system above the isotropic-nematic phase transition. The rapid motion of the tip sonicator formed droplets of varying sizes in a very small amount of time. Isotropic droplets were then cooled to the nematic phase using two different cooling rates: 1 °C/min and ~200 °C/min, and quantum dot cluster formation and location were observed using a fluorescence microscope.

Fluorescence microscopy was used to image the spatial distribution of quantum dots in the liquid crystal droplets. In the experiments presented CdSe/ZnS core shell quantum dots (NN Labs) with an emission peak of 620 nm were used. Fluorescence images were carried out on an upright Leica DM2500P microscope in reflection mode using a 20x objective. A white-light mercury lamp illumination source with a 515-560 band-pass filter was used for quantum dot excitation. Emission was detected using a 580 nm dichroic mirror and a 590 nm long pass filter. The microscope can also be used in transmission mode with a white light source and crossed polarizers to image birefringence. The droplet suspensions were mounted on standard glass slides under a cover slip for observations.

3.3 Results

3.3.1 Slow Cooling Experiments

Through our experiments, we utilize two different molecular orientations for the droplets: radial and bipolar. Schematics for these molecular orientations are shown in Figure 22. In our first set of experiments, the liquid crystal droplets with dispersed quantum dots were cooled at 1 °C/min. Experiments were carried out at two different concentrations of quantum dots: 0.05 wt % and 0.2 wt %. The lower concentration was specifically chosen to prevent spherical shells and other macroscopic structures from forming via the transition templating process, as recently reported for the same system in bulk at concentrations above ~0.15 wt % [46, 48], and to obtain a small cluster. Figure 23 shows our results from the slow cooling experiments in which we compared radial and bipolar droplet configurations. Radial droplets resulted in quantum dot clusters localized at the hedgehog defect at the center as shown in Figure 23a. Co-localization was verified using a combination of both fluorescence and cross-polarized microscopy. Cluster sizes varied droplet to droplet, with larger droplets producing larger central clusters. This result is expected, assuming that all droplets begin with a uniform dispersion of quantum dos and that these dispersed droplets all end up at the central defect after the liquid crystal transitions to the nematic phase.

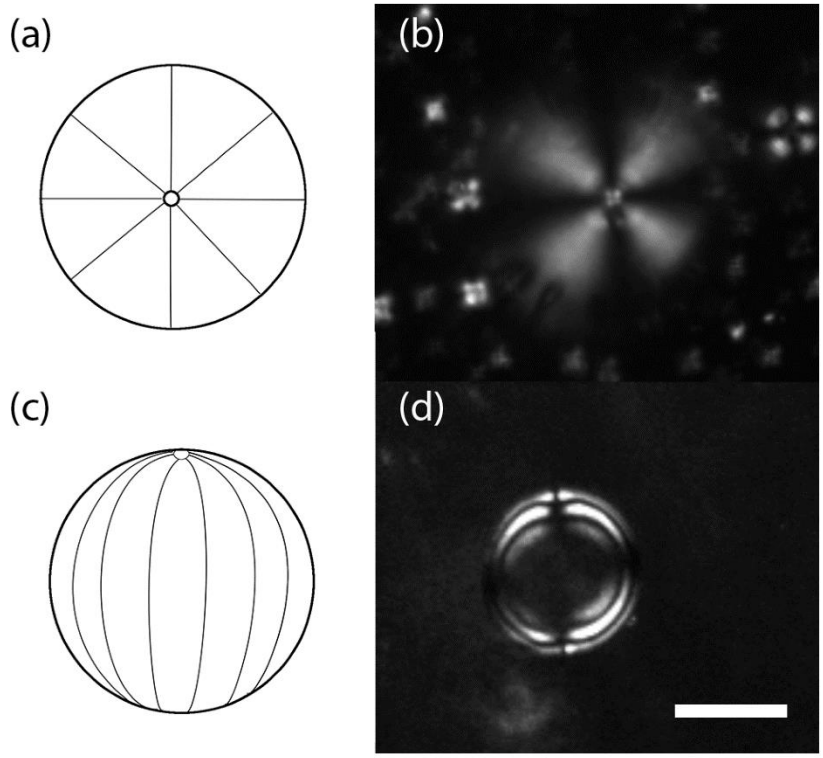

Figure 22: Two common director configurations for a nematic liquid crystal droplet. Radial (defect at the center); (a) schematic and (b) crossed-polarizer image of a droplet suspended in aqueous solution, and bipolar (two surface defects); (c) schematic, and (d) crossed-polarized image of a droplet suspended in glycerol. Scale bar = 20 mm.

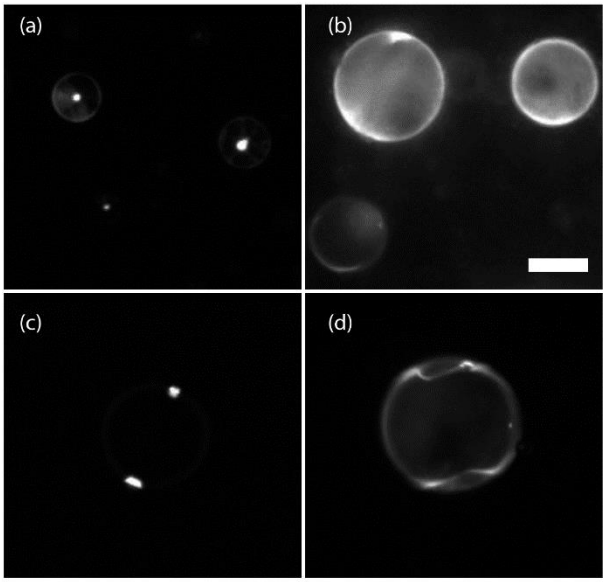

Figure 23: Examples of quantum dot clusters formed via slow cooling of nematic droplets. (a) Clusters located at the center of a droplet, with the liquid crystal in a radial configuration; (b,c) Two different examples of quantum dot distributions in bipolar droplets at a low particle concentration and (d) at a higher particle concentration (For all images, bar = 20 μm)

3.3.2 Rapid Cooling Experiments

In a second series of experiments we repeated the procedure described above, but with a significantly faster cooling rate of ~200 °C/min. This rapid cooling rate was chosen to match that used in recent experiments where we reported the formation of spherical quantum dot shells by phase transition templating [47]. We first tested the low concentration quantum dot - 5CB mixture (0.05 wt %) using homeotropic boundary conditions, and again saw quantum dot clusters forming at the center hedgehog defect. However, when droplets cooled with planar boundary conditions were examined, we observed a surprising result—the quantum dot cluster also formed at the center (Figure 24a)—in contrast to the surface-localized particles exhibited for low cooling rates in Figure 23. Using cross-polarized microscopy, we observed that the cooled droplets in fact had radial defect conformations, not the expected bipolar conformation (Figure 23c for example). This result clearly indicates that within

the appropriate parameter range, phase front sorting dominates the assembly process over the slower topological defect assembly process.

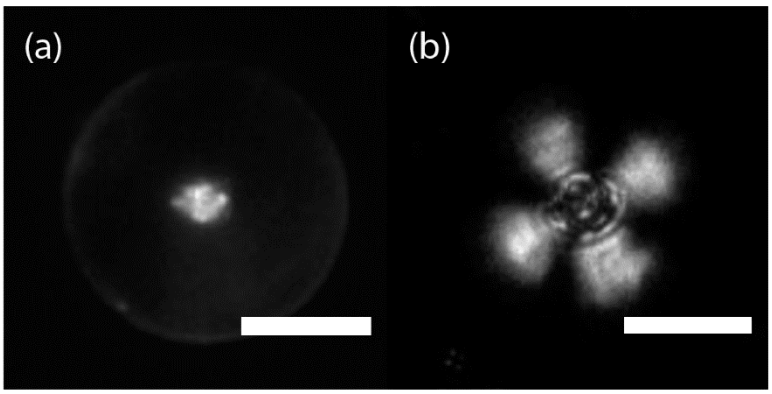

Figure 24: Quantum dot cluster imaged using (a) fluorescence microscopy and (b) cross-polarized bright field microscopy at the center of a droplet designed to exhibit the bipolar defect configuration. After cooling to the nematic phase, particles were found to be located at a single central point in the radial defect configuration. Scale bars = 20 μm.

We then tested the same fast cooling rate at the higher concentration of QDs in 5CB (0.2 wt %). Cooling these radial droplets produced hollow microshells located at the droplet centers. These microshells are identical to those discussed in publications [47]. However, in this case, we demonstrated that it is possible to form a single hollow shell in the center of a liquid crystal droplet (Figure 25). While the previously reported bulk method for microshell formation is limited by spatial control, this new method provides a mechanism to form individual microshells at specified locations—that is, at the center of LC droplets.

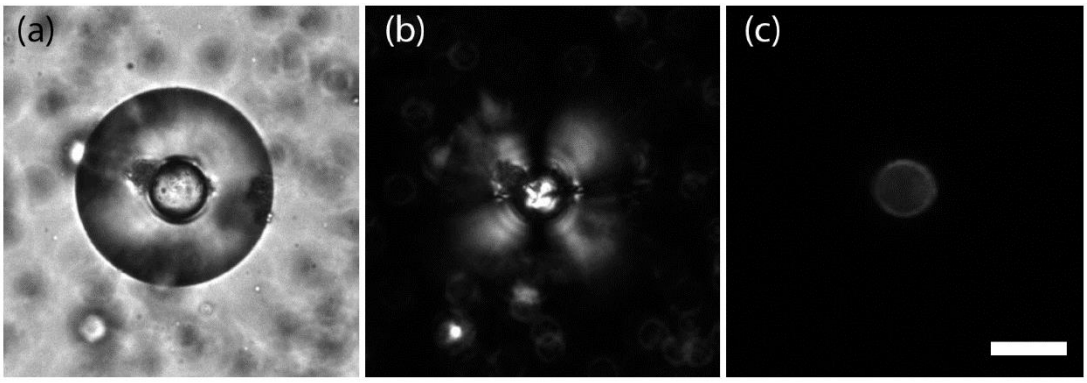

Figure 25: Optical microscopy images of the same droplet with a single quantum dot hollow capsule inside. (a) Bright-field image; (b) cross-polarized image; and (c) fluorescence image, showing quantum dots only. Scale bar = 20 μm.

3.3.3 Cluster Analysis

To quantify the clustering formation process we carried out a scaling analysis for the phase transition sorting mechanism that produced the central cluster, as shown in Figure 24. Clustering via the two different formation mechanisms produces particle packings that are quite different. Slow particle assembly by cluster-cluster aggregation and subsequent topological defect localization is expected to produce fractal-like packing with a mass-scaling dimension of 1.8 [75]. In contrast, the phase front templating method has been shown to produce very dense amorphous particle assemblies, including the micro-shells we demonstrated in Figure 25. A notable benefit of forming quantum dot clusters in the confined geometry of a droplet is that it gives us the ability to quantify their spatial characteristics—since we know the concentration of particles and the droplet size, we can estimate the mass of quantum dots in each droplet. We can characterize a cluster of nanoparticles by its fractal dimension, *D*, where the relation between the mass of an object and its size is given as

$$M = Ar^D \tag{31}$$

where M is the mass of the object, A is a constant, and r represents the radius of the cluster. To calculate the mass-scaling dimension of nanoparticle clusters, we measured cluster size as a function of cluster mass.

In the perfect case, all particles in a droplet would be driven to the central point, and the mass of a specific cluster would simply be obtained as $M = c\frac{4}{3}\pi r^3$, where c is the initial particle concentration before the phase transition (in the isotropic phase) and R is the radius of the droplet. However, we observed that droplet images under fluorescence microscopy indicated some emission in regions other than the central defect. This leads to the conclusion that not all of the nanoparticles were swept up during the isotropic–nematic phase transition and that some remain dispersed in the nematic phase. When estimating the mass scaling dimension of our clusters, we corrected for this effect to obtain more accurate measurements of the cluster mass. To calculate a ratio of the number of nanoparticles in the cluster compared to the number of nanoparticles in the bulk droplet, fluorescence intensity was integrated over the entire droplet using ImageJ and a corrected cluster mass calculated. In addition, background fluorescence away from the droplet was measured and subtracted to account for background noise.

Droplet and cluster diameters were measured using bright field and fluorescence microscopy. To measure cluster diameters, three pixel-wide intensity line profiles were measured from fluorescence images and fitted with a Gaussian profile (Figure 26a). The diameter of the cluster was taken as the full-width half-max of the profile.

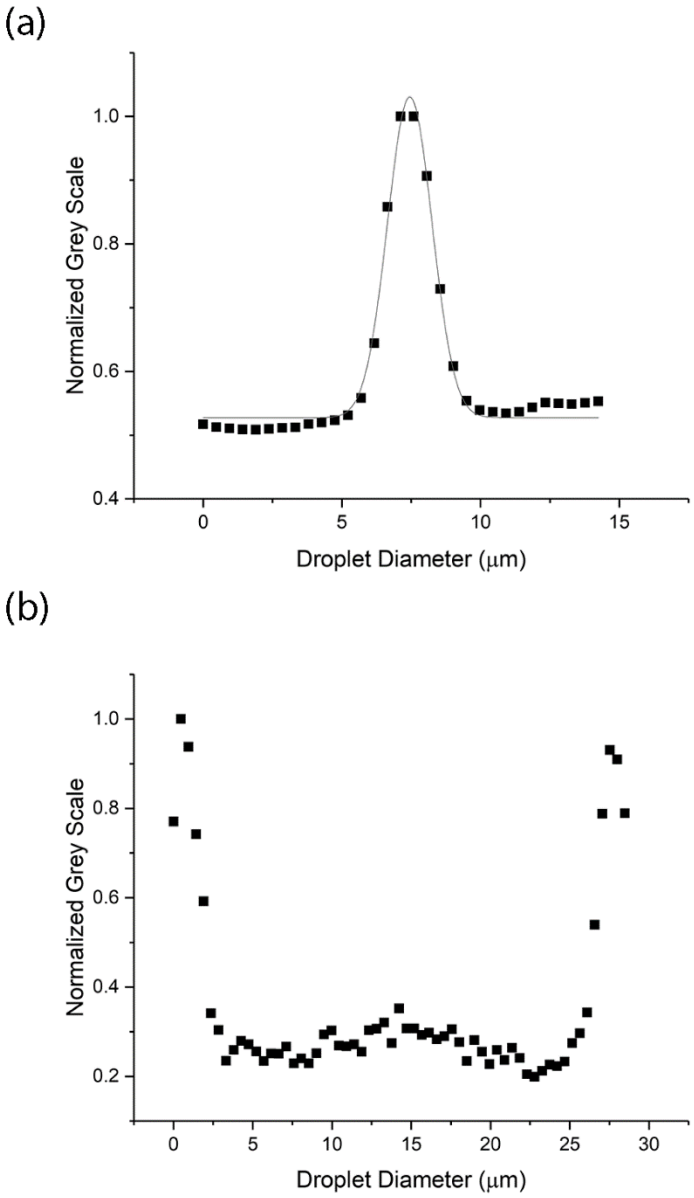

Figure 26**:** Fluorescence intensity measurements across quantum dot clusters in a droplet as determined using a one-dimensional (1D) line profile across the microscope image. (a) Radial droplet example measured across the central cluster (as shown in Figure 22a) showing a peak intensity at the center of a droplet with Gaussian fit; (b) Similar data for a bipolar droplet measured across the surface clusters (as shown in Figure 22c) showing two peak intensities at opposite poles of the droplet.

The volume of each droplet was determined, and finally the mass of the droplet was determined using the density of 5CB. Since we know the mass of the 5CB droplet and the quantum dot concentration by wt %, we can calculate the total mass of quantum dots in each droplet. With the mass and size of the quantum dot clusters, the packing fraction can be obtained. Figure 27 shows cluster mass as a function of cluster radius for an ensemble of different quantum dot clusters formed using the phase front assembly method (rapid cooling, lower concentration). In this plot we assumed a 5% variation on the concentration of quantum dots in isotropic 5CB. The chi-square test resulted in a value of 21. Although not an excellent fit to the data, which exhibits significant scatter, this fit allowed us to quantify the linear trend, observed visually. The slope of this fit represents a scaling dimension of 2.5 ± 0.4, which is relatively dense and consistent with the theoretical value for three-dimensional (3D) ballistic aggregation [75, 76].

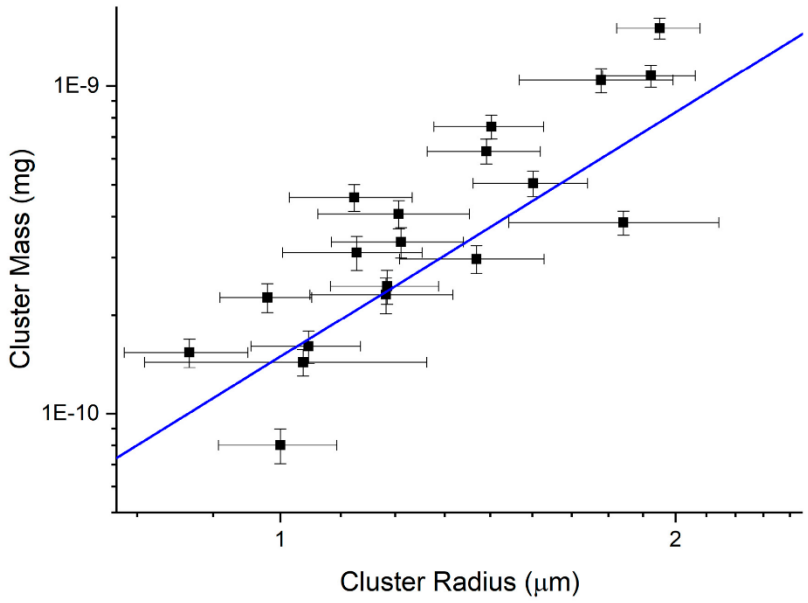

Figure 27: Calculated cluster mass plotted as a function of measured cluster radius. Log–log plot of Equation (1) fit to experimental data. The data collected were cluster mass and cluster size. The straight line fit on a log–log plot indicates a mass scaling dimension of 2.5 ± 0.4.

3.4 Discussion

Our initial hypothesis was that QD cluster patterning would be achieved through equilibrium defect formation in a liquid crystal droplet in a similar mechanism to that recently reported for micron-scale particles [61]. However, we also proposed that rapid cooling might lead to the formation and stabilization of out-of-equilibrium structures such as the recently reported QD spherical shells reported at high cooling rates in a similar system [47]. To investigate these mechanisms, we carried out two sets of experiments, focused on slow cooling and rapid cooling through the isotropic to nematic transition. The droplet geometry was particularly useful in these experiments because the ground-state topological defect configurations are well defined. In addition, the particle concentration within the droplet is easily controlled.

3.4.1 Two Different Mechanisms for Assembly

In this paper we considered two separate mechanisms responsible for the spatial organization of particles in liquid crystal droplets. Overall, the collection of quantum dots occurred at the defect location (i.e., center) of the droplet by a simple free energy argument. There are three major contributions to the free energy for quantum dots inside a liquid crystal droplet: elastic forces, phase transition dynamics (Landau theory (order parameter)), and the actual insertion of quantum dots. This can be expressed as $F=F_{el}+F_{L}+F_{QDs}$. The elastic free energy is the classic Frank Free energy which consists of splay, twist, and bend energies; these are the common deformations of a liquid crystal. The Landau free energy governs the phase transition, and the quantum dot free energy can be considered to represent the particle fraction inside the liquid crystal medium. The particles are swept up due to the changes governed by F_L, and the location is then governed by the elastic forces that could possibly move the formed cluster to defect locations.

In the first mechanism, “equilibrium defect assembly”, the transition particles assemble in the topological defects, producing an 3D aggregate with a fractal-like mass scaling. This is consistent with previous observations in bulk liquid crystal. Given sufficient time, particles initially not located at defects will eventually migrate there by thermal motion and “fall in” to the aggregate. This process is most likely to occur at very low particle concentrations.

The second mechanism is through "phase transition assembly". In this mechanism, particles preferentially locate in a shrinking isotropic domain within the droplet as it cools through the isotropic to nematic phase transition. The particles are pushed close together as the isotropic phase shrinks to form a cluster.

The first mechanism for nanoparticle sorting in the droplets concerns their tendency to cluster and localize at topological defects in the liquid crystal. Spherical particles of all sizes have been shown to accumulate at defect points in liquid crystals. This is a relatively slow size-dependent process, whereby particles in the nematic phase tend to locate at points of low order to minimize the elastic deformation of the liquid crystal by radially symmetric particles.

The second mechanism is related to the propagation of the isotropic to nematic phase front. In this case, particles preferentially locate in shrinking isotropic domains at the phase transition and are effectively pushed together by the nucleating, growing nematic domains, entropically repelled by the ordered environment of the nematic phase. This sorting process can occur rapidly and, if the particles are small enough, provides an excellent mechanism to assemble nanoparticle-based structures.

In all droplets, we started with a uniform particle distribution in the isotropic liquid crystal phase. Then, following a cooling step, the liquid crystal transitioned into the nematic phase. Our results highlight several possibilities for controlling particle organization.

Using different cooling rates, we observed evidence of competition between the two different assembly mechanisms. Six-nanometer nanoparticle diffusion in the nematic phase can be generally considered as an Brownian random walk, modified by local director orientation. Particles and small clusters will explore the droplet until they locate in a topological defect. We can characterize this motion by timescale, τ_{QD}, the time for a particle to travel a mean squared displacement (MSD) equal to the radius of the droplet.

As nanoparticles and small clusters of particles move randomly, they may encounter other particles or clusters, increasing their size. This will further slow their diffusion rate, increasing $\tau_{QD,}$ and thus can be described as cluster-cluster aggregation in an anisotropic environment. Slow cooling the droplet through the phase transition tends to produce many small nematic domains which nucleate

and grow. At slow cooling rates this process does not appear to impact the migration of the nanoparticles to topological defects, either at the center of a radial droplet, or on the surface of a bipolar droplet (Figure 22a,c).

Rapid cooling through the phase transition allows the second assembly mechanism to dominate. In this case we typically observe a single-phase front rapidly moving across the droplet. If the phase front transition timescale, τ_{PF} (the time for the phase front to travel the radius of the droplet) is short compared to the QD clustering timescale ($\tau_{PF} < \tau_{QD}$), we expect the phase front particle sorting to dominate over Brownian motion. A simple analysis supports our assumptions. The diffusion constant of a quantum dot in isotropic 5CB was estimated to be 4 $\mu m^2/s$. This was obtained from viscosity measurements from [77] and from using the Einstein–Stokes relation for diffusion, with T above the isotropic–nematic phase transition point. These values yield a linear diffusion length for the QDs of ~5 μm/s in a 3D droplet. To quantify the phase front timescale (τ_{PF}), we analyzed a 60-μm diameter droplet and measured the phase front velocity to be 27 μm/s. These numbers illustrate that we can expect the phase front to move approximately five times faster than the linear diffusion of an average QD in the nematic phase.

We can relate the phase transition assembly process to a non-quasistatic compression. In the case that phase transition assembly dominates, the particles are not able to diffuse away before being swept up by the phase boundary. The particles then follow the direction of the phase front, which depends on the temperature gradient direction in the liquid crystal droplet. If all of the particles are swept up, and the cluster is of sufficient size compared to the size of the droplet, Frank elastic effects are insufficient to move the large cluster, and so the liquid crystal will reorient itself around the cluster to minimize the free energy of the system. This reorientation may not always be the lowest energy state possible, as seen with the surprising example of a cluster stabilized at the center of a bipolar droplet (Figure 24). This phase front aggregation process could be described as a ballistic diffusion-limited aggregation process as particles are pushed together in the shrinking isotropic domain.

3.5 Conclusions

In this Chapter we investigated the spontaneous assembly of nanoparticle clusters in the confined environment of a liquid crystal droplet using mesogen-functionalized quantum dots. Varying surface anchoring conditions at the droplet/water interface allowed us to tune between radial and bipolar topological defect configurations. By tuning particle concentration and cooling rate across the isotropic to nematic phase transition, it was possible to observe the competition between two distinct assembly mechanisms: equilibrium defect assembly and phase transition assembly. We observed two key effects. First, slow cooling allows for ground state defects to template quantum dot cluster formation, while fast cooling allows for the isotropic–nematic phase boundary to template the clusters. Secondly, we noticed that phase transition templating can be used to force non-equilibrium defect configurations, such as a radial director distribution, despite initial bipolar anchoring conditions. This droplet technique also provides a method to control quantum dot micro-shell (and cluster) formation location, opening the possibility for easy spatial control of micron-scale nanoparticle assemblies.

The contents presented in this chapter have been published.
Charles N. Melton, Sheida T. Riahinasab, Amir Keshavarz, Benjamin J. Stokes, and Linda S. Hirst. Phase Transition-Driven Nanoparticle Assembly in Liquid Crystal Droplets. *Nanomaterials*, **2018,** 8, 146

Chapter 4

Characterizing Quantum Dot Micro-Shells in a Liquid Crystal Droplet

4.1 Introduction

Quantum dot, nanosized semiconductors, have proven useful for numerous applications, such as optoelectronic devices, drug-delivery systems, and biochemical sensors [6-10]. These nanocrystals can be considered zero dimensional and are produced with an approximately spherical shape with diameters ranging from 1-12 nms. Quantum dot emissions largely vary in wavelength, emitting longer wavelengths in a lower energy but more defined emission band. Decreasing the size of the quantum dot results in an increase in the energy level spacing, thus the emitted wavelength depends on the size of the quantum dot.

Self-assembly of nanoparticles using a liquid crystal matrix has shown to be a reliable way of forming several types of structures. These structures range from small arrays of nanoparticles to complex clusters and hollow micro-shells. The self-assembly mechanisms that govern these structures vary, from topological defect assembly to phase-transition templating.

In this Chapter we pursue the phase-transition templating method of self-assembly to produce and characterize hollow quantum dot micro-shells in a confined liquid crystal geometry. The geometry of choice is a liquid crystal droplet. Using droplets produce singular self-assemble structures, allowing for easy characterization of the material. The formation of single quantum dot micro-shells will allow for spatial control of the formation process and open the way to possible device applications.

4.2 Methods and Materials

We begin by functionalizing quantum dots with a flexible mesogenic ligand, similarly as previously reported [47]. The mesogenic ligand replaces octadecylamine surface ligands on commercial CdSe core / ZnS shell quantum dots (NN Labs Inc.). This ligand allows for improved particle dispersion in the host liquid crystal matrix (4-cyan-4'-pentylbiphenyl, "5CB"), and produces a uniform dispersion of modified QDs in the isotropic phase.

After surface modification, the QDs are uniformly dispersed in 5CB via heat bath sonication at 50 °C for 2 hours, then verified by fluorescence microscopy. After sonication the mixture is held in an oven at 50 °C. The particle concentration used is 0.2 wt%. This concentration allows for quantum dot micro-shell formation during the isotropic-nematic phase transition.

Once a uniform particle dispersion in 5CB is achieved droplets can be formed. We pipette 3 μL of QD-5CB composite into 300 μL into Millipure water. After pipetting, the system was then sonicated using a cell disrupter for approximately one second, until the resulting emulsion appeared cloudy, keeping the system above the isotropic-nematic transition temperature. Isotropic droplets were then cooled into the nematic phase as previously reported[6], forming hollow micro-shells at the center of the droplet.

Fluorescence microscopy was used to image the micro-shell inside each nematic droplet. Fluorescence imaging was carried out on an upright Lecia DM2500P microscope in reflection mode using a 40x objective. A white-light mercury lamp illumination source with a 515 – 560 nm band-pass filter was used for QD excitation. Emission was detected using a 580 nm dichronic mirror and a 590 nm long pass filter. The microscope can also be used in transmission mode with a white light source and crossed polarizers to image birefringence. The droplet suspensions were mounted on standard glass slides under a cover slip for observations.

4.3 Results

Figure 28 shows a single quantum dot micro-shell at the center of a nematic liquid crystal droplet. Figure 28a shows a bright-field image of one such droplet with a micro-shell at the center. Figure 28b shows the corresponding crossed polarized image, and Figure 28c shows the shell under fluorescence microscopy.

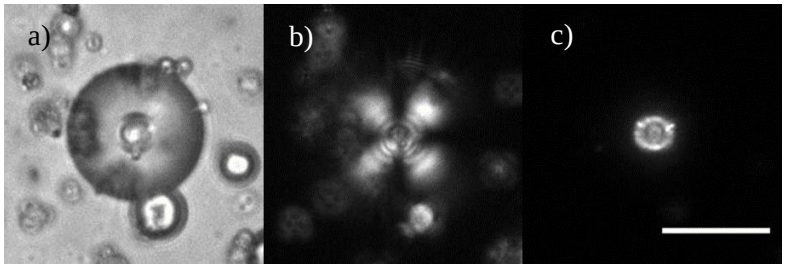

Figure 28: Optical microscopy images of a 5CB droplet with a single quantum dot hollow capsule. (a) bright-field image (b) cross-polarized image, and (c) fluorescence image, showing quantum dots only. Scale bar = 20 μm.

Shell diameters were measured inside each droplet, along with the diameter of the corresponding droplet, and plotted in Figure 29. The data shows a linear trend between droplet size and shell size, showing a direct correlation between the two. The fit is done with a slope of 1.5 and an R^2 value of 0.9. From this we can deduce a mathematical relation between droplet size and shell size. This equation is

$$D_D = 1.51\, D_s + 3.33\ \mu m \tag{32}$$

where D_D is droplet diameter and D_S is the shell diameter. We deduce form this a minimum droplet size to form shells. That size is ~ 3 μm. Droplet and shell diameters were also tabulated in Table 1.

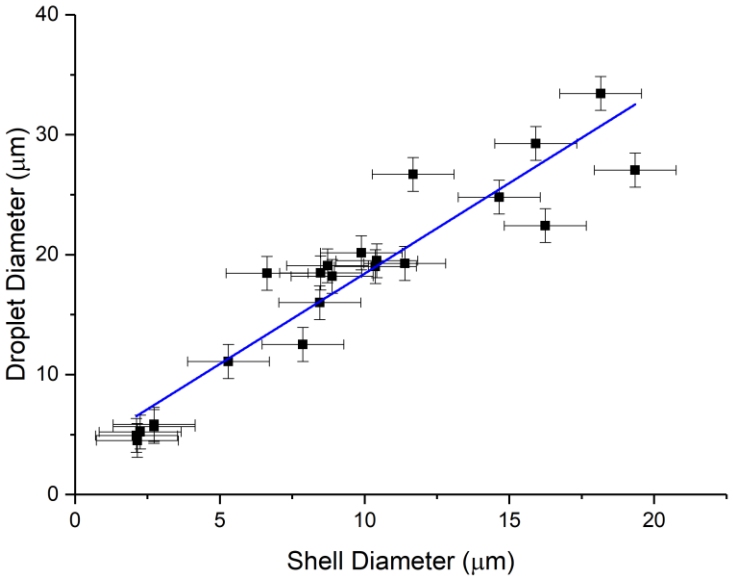

Figure 29: Plot of Droplet Diameter vs. Shell Diameter. The data is fit with a slope of 1.5, indicating a set scaling behavior between droplet size and shell size.

Table 1: Shell and Droplet Diameter measurements, and their corresponding ratio. We obtain an average droplet to shell size ratio of 1.98 ± 0.16, again indicating a set scaling factor between shell size and droplet size.

Shell Diameter (μm)	Droplet Diameter (μm)	Droplet/Shell Ratio
15.91	29.27	1.84
10.37	19.01	1.83
11.67	26.69	2.29
14.65	24.80	1.69
11.39	19.27	1.69
10.42	19.50	1.87
5.29	11.09	2.09
2.25	5.22	2.32
2.12	4.93	2.32
2.15	4.51	2.10
2.73	5.67	2.08
2.73	5.85	2.15
8.48	18.48	2.18
16.24	22.42	1.38
8.88	18.19	2.05
7.87	12.51	1.59
19.35	27.05	1.40
9.88	20.15	2.04
8.45	16.00	1.89
8.72	19.08	2.19
18.15	33.44	1.84
6.63	18.45	2.78

Another advantage of the confined formation of quantum dot micro-shells allows for the characterization of wall thickness. Confined geometries allow for the estimation of total number of quantum dots in the system since initial concentration is known. Wall thickness is determined through a simple calculation. The schematic of the system is shown in Figure 30.

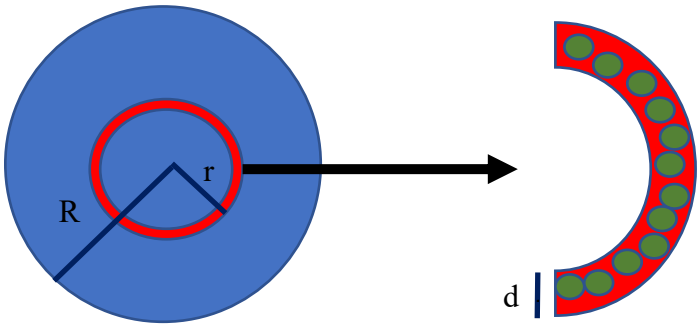

Figure 30: Schematic of QD micro-shell inside a 5CB droplet. The droplet possesses radius R, shell radius r, and shell thickness d. The shell wall is composed of packed QDs.

Assuming all the particles are swept to the center of the droplet through the isotropic-nematic phase transition, the total volume of the quantum dots can be compared to the volume of the shell:

$$NV_{QD} = f(V_{out} - V_{in}) \tag{33}$$

Where V_{QD} is the volume of a quantum dot, f is the packing fraction (assuming the quantum dots are spherical in shape), and $V_{out} - V_{in}$ is the effective volume of the shell. The number of quantum dots, N, in a given volume can be calculated by knowing the concentration of quantum dots in the liquid crystal per unit volume. Rewriting Equation 33 using the droplet radius R, the shell radius r, and shell thickness d into

$$aR^3 = f(r^3 - (r-d)^3) \quad (34)$$

The constant a is defined by $\frac{c_{QD/5CB}}{\rho_{Cd/ZnS}}$, where $c_{QD/5CB}$ is the mass per unit volume concentration of quantum dots in 5CB, and $\rho_{Cd/ZnS}$ is the density of a quantum dot. For this work, a = 0.00319. Figure 31 shows droplet and shell measurements fitted to Equation 34 with a packing fraction of 0.74. The fit estimates a shell thickness of 44 ± 4 nm, with an R^2 value of 0.82.

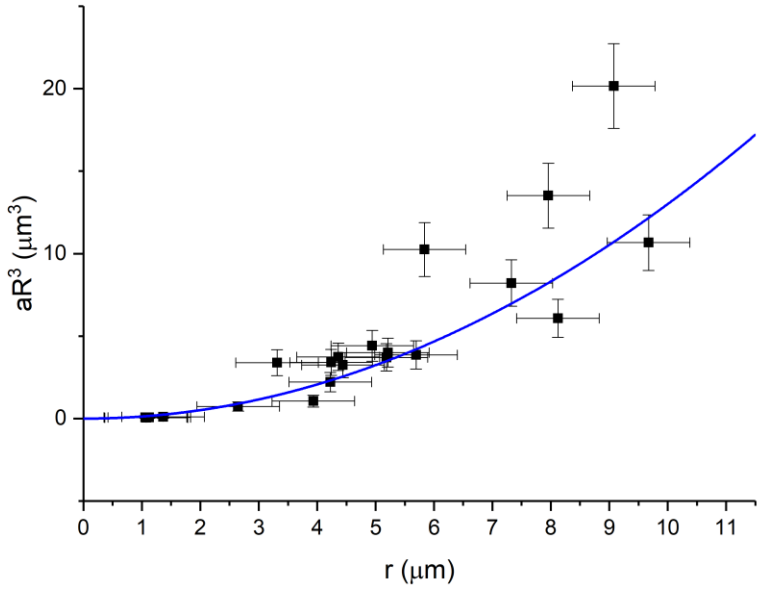

Figure 31: Plot of droplet radius vs shell radius, fitted using equation (2). The fitting parameter d is 44 ± 4 nm.

4.4 Discussion

The initial hypothesis of these experiments was that confinement will dictate where shells form in a liquid crystal host, and that these droplet sizes will control shell size. Experiments have shown that confinement does indeed control where shell form in the liquid crystal, benefiting from the geometry-dictated topological defect.

By confining the quantum dots to a space of a fixed size (the size of the droplet), the size of the formed micro-shell can be reliably predicted. Figure 29 shows that there is a direct relation between shell size and droplet size. When considering the set quantum dot concentration inside the liquid crystal droplet, it is reasonable that the formed shells would sit within a certain size regime. Consider a droplet of diameter *R*. Within this diameter is a set number of quantum dots. Upon being swept up via the isotropic-nematic phase transition, the quantum dots eventually arrest and can no longer pack closer together. Thus, the concentration dictates the initial cluster size. The only way for this cluster size to increase is if there are more quantum dots, and that occurs in larger droplets, following the set concentration.

A major implication of this data analysis is that there exists a minimum droplet size needed to form a shell. Setting $Ds = 0$ in Equation 32, there is a minimum droplet size of 3.33 μm. This suggests there is a minimum amount of quantum dots needed to be present to form a shell. This agrees with Reference 47 stating that a minimum concentration of quantum dots is needed to form a single micro-shell. It is perhaps possible that even though a single droplet may have enough quantum dots by volume to form a shell, a size restriction exists that prevents extremely small shells form forming.

By utilizing the droplet confinement of shell formation, shell thickness can also be controlled. Increasing concentration within droplets of equal size will result in thicker shells, as the size of the droplet provide a limit for how large a shell can be.

4.5 Conclusion

In conclusion quantum dot micro-shells are successfully formed inside nematic liquid crystal droplets. Shell size has been shown to be directly related to droplet size, which is consistent with various system sizes held at a constant concentration. Parameters such as shell thickness and shell size are highly tunable via concentration of quantum dots in the liquid crystal. This will allow for more control over quantum dot micro-shell formation processes to allow for wanted variations.

Chapter 5

Simulations of Nematic Liquid Crystals and Phase Separation

5.1 Introduction

As 5CB undergoes its phase transition from isotropic to nematic, the transition is not instantaneous. Nematic domains nucleate and grow, while isotropic domains shrink. If 5CB has been doped with quantum dots, as previous chapters have discussed, the quantum dots are expelled from regions of nematic order and follow the shrinking isotropic domains. Further experimentation has shown that these domains may end up being larger or smaller depending on the cooling rate used to initiate the phase transition. This is the case for the quantum dot micro-shells where it is hypothesized that cooling rate affects final shell size [47].

This Chapter is dedicated to the discussion of a model which replicates the physics observed in experiment. Advantages of the model is to easy vary system size, concentration ratios of particle to 5CB, and cooling rate. Being able to easily change these parameters provides an advantage to experimentation of being able to quickly change parameters and study system responses.

To model the liquid crystal a spin model will be used. As introduced in Chapter 2, spin models have been a powerful tool in modeling nematic alignment, and the Lebwohl Lasher model [70] exhibits a first-order phase transition. To model phase separation the Cahn- Hilliard equation will be used [78]. The specifics of these models will be discussed in the following sections.

5.2 Liquid Crystal Model

In this section the spin model used for the liquid crystal will be discussed. The free energy of a nematic liquid crystal was stated in Equation 9. The free

energy, following the one constant approximation and in terms of the Q tensor is [79]

$$f = \frac{K}{4} G_1 \tag{35}$$

where

$$G_1 = Q_{jk,l} Q_{jk,l} = 2((\nabla \cdot \vec{n})^2 + (\vec{n} \cdot \nabla \times \vec{n})^2 + (\vec{n} \times \nabla \times \vec{n})^2) \tag{36}$$

The proposed model will be discretized to a lattice. To calculate the free energy of the model the free energy density in Equation 35 will need to be integrated over a volume. The integral can be discretized to a sum over nearest neighbors on the lattice and be written as

$$F = \int \frac{K}{2} G_1 dV = \sum_{<a,b>} \frac{K}{2} (Q_{jk}^b - Q_{jk}^a)(Q_{jk}^b - Q_{jk}^a) \tag{37}$$

Rewriting Equation 37 in terms of Equation 2 (the relation between the Q-tensor the nematic director) we obtain [79]

$$F = \frac{K}{2} \sum_{<a,b>} (1 - (\overrightarrow{n_a} \cdot \overrightarrow{n_b})^2) \tag{38}$$

By writing the free energy in terms of the nematic director the degrees of freedom are reduced from five to two, which reduces computation time. Spins that represent the nematic director will interact using Equation 38. The system will move forward in time by

$$\vec{n}_{i+1} = \vec{n}_i + (\vec{\omega}_i \times \vec{n}_i) \Delta t \tag{39}$$

The rotational velocity $\vec{\omega}_i$ is proportional to the torque applied to a spin due to the spin's corresponding neighbors which is given by

$$\vec{\tau}_i = K \sum_b (\vec{n}_i \cdot \vec{n}_b)(\vec{n}_i \times \vec{n}_b) \tag{40}$$

which is derived from the variation of the free energy density. To induce the phase change in the system, the temperature will be implemented via a Langevin heat bath, given by Equation 24.

To fully summarize this spin model, spins on an N×N×N lattice represent the local nematic director at a coarse-grained level. The interaction energy is summed over nearest neighbors with periodic boundary conditions. The spins evolve forward in time using Equation 39 by calculating the torque on a spin due to its neighbors. Temperature is controlled via a Langevin thermostat. The model will be run at various cooling rates. To quantify nematic order, the nematic scalar order parameter is calculated by finding the largest eigenvalue of the Q tensor, averaged over a radius of two lattice spaces.

Results of the model are shown in Figure 32. Figure 32 shows a slice through the bulk of a 3D volume of spins. The spins at the boundary were held fixed. Through this slice we see a combination of nematic alignment and topological defects. The defects have a charge of ± 1/2. This combination of defects and alignment suggests this snapshot is of the nematic phase. Figure 33 shows the calculated order parameter of the bulk for this specific simulation. The order parameter was calculated at each temperature step. We see at kT = 0.5 there is a sudden jump in order, indicating the presence of a first order phase transition. The presence of this transition indicates the model serves well to replicate a nematic liquid crystal.

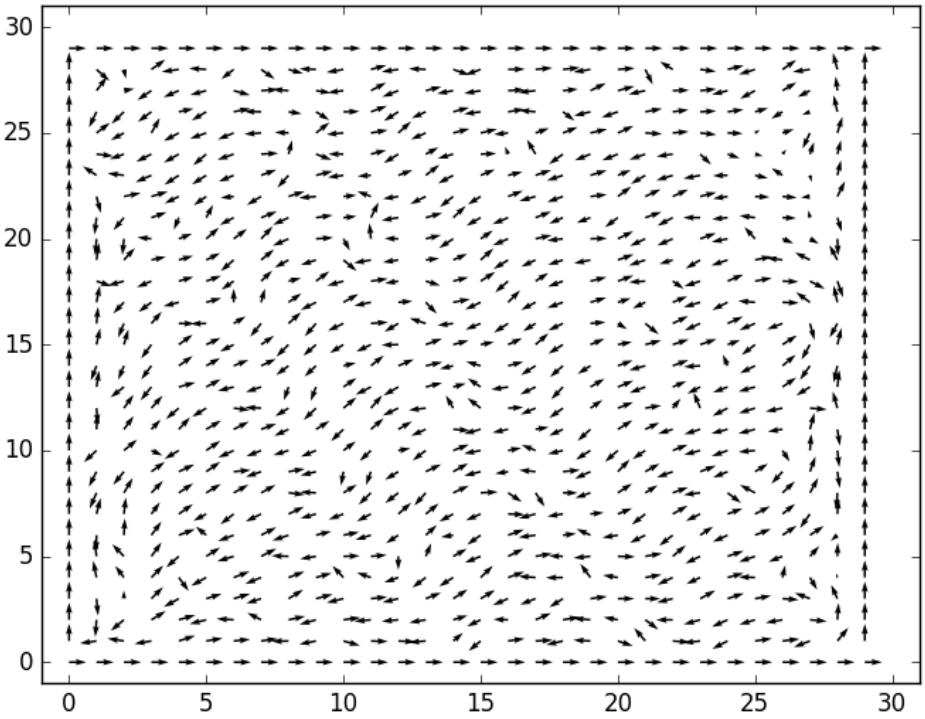

Figure 32: Slice of a bulk nematic liquid crystal spin system. Note the presence of both topological defects and nematic ordering.

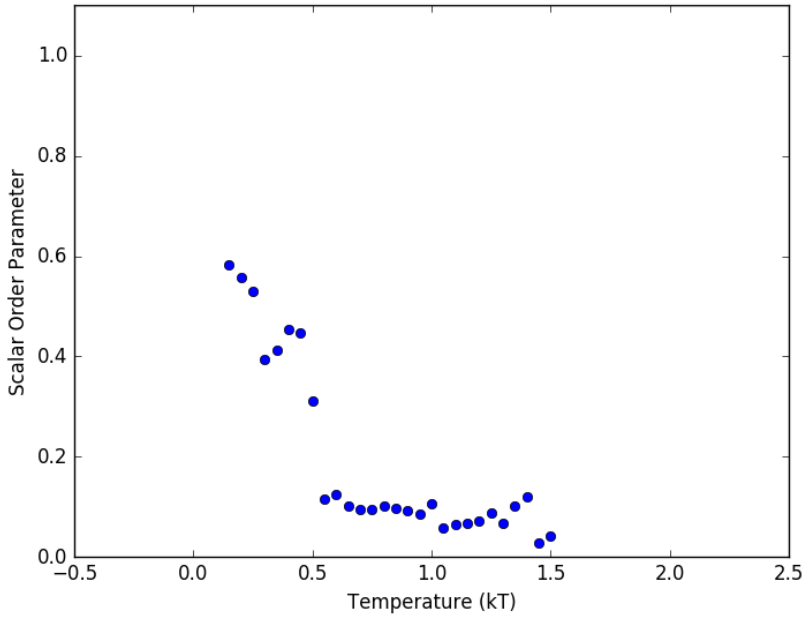

Figure 33: Plot of the nematic order parameter as a function of temperature. A discontinuity exists at kT = 0.5.

5.3 Phase Separation Model

To model the separation of nucleating nematic domains and shrinking isotropic domains, the Cahn Hilliard model is used. Cahn Hillard describes the separation of two immiscible species. The two species are treated as densities: this does not describe the separation of individual particles. The Cahn Hillard model is given by

$$\frac{\partial c}{\partial t} = D\nabla^2(c^3 - c - \gamma\nabla^2 c) \tag{41}$$

Here, c represents the range of densities. The values range between +1 and -1. The $c^3 - c$ term is derived from the variation of a double well potential with minima at +1 and -1. This potential is plotted in Figure 34. The $\gamma \nabla^2 c$ term penalizes the mixing of the two values of c.

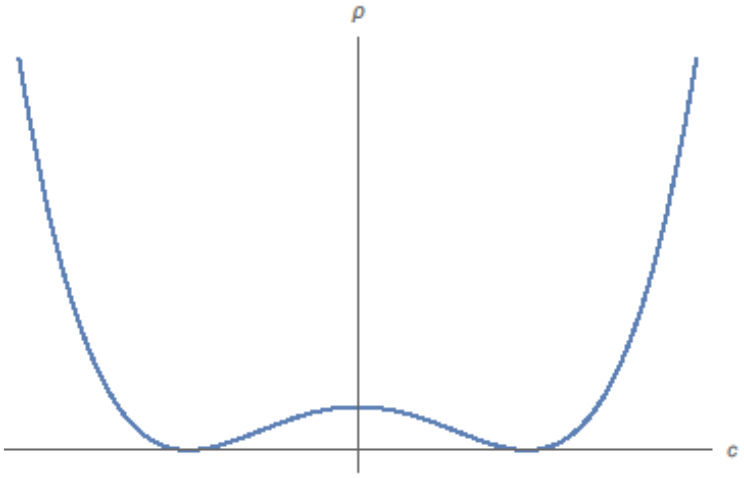

Figure 34: Plot of the double well potential for the Cahn Hilliard equation. Two minima exist to drive the separation of two species.

Results of the solutions to Equation 38 are shown in Figure 35. For this specific run, the system was 2D. The two colors presented, red and blue, represent the two immiscible species. The simulation was ran for a certain number of time steps till this degree of separation was achieved. The simulation could have run for longer, until only two separate domains remained (think oil separating from vinegar in a salad dressing). This same simulation can easily be computed in 3D and will be done so to model the phase separation occurring in the nematic spin model. The cooling rate controlled by the Langevin thermostat will be changed to study the effect of cooling rate on final particle-rich domain size.

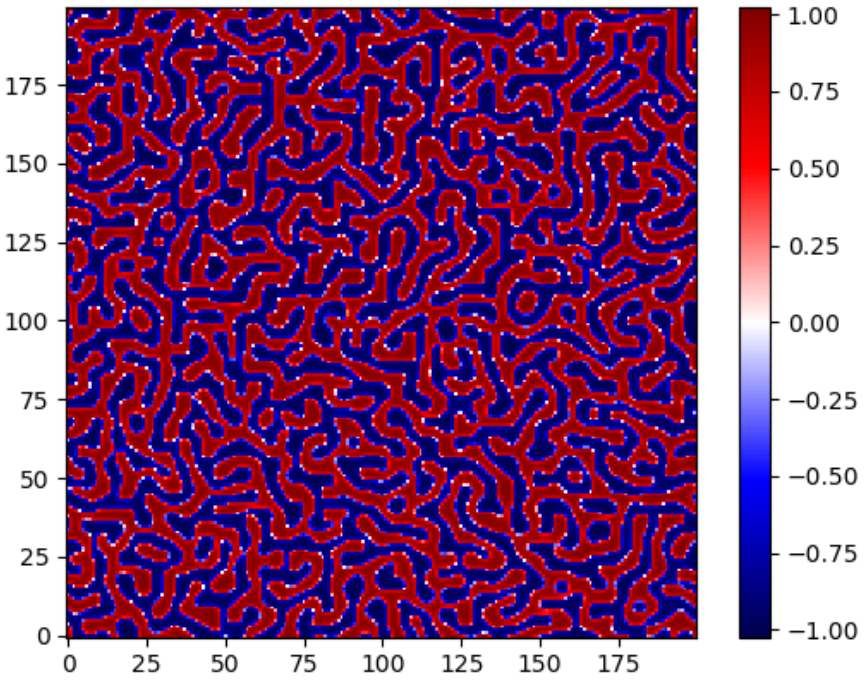

Figure 35: Results of the solution to the Cahn Hilliard equation. The red and blue represent the density of the two immiscible fluids.

To fully represent the separation of the particle-rich isotropic domains from the nematic domains, we need to include a specific driving term. Experimental data from Reference 46 highlights this separation of particle-rich domains from nematic domains (Figure 36). This separation is credited to the presence of an order parameter. Considering this order parameter as a driving term, Equation 41 is adjusted to the form

$$\frac{\partial c}{\partial t} = D\nabla^2(c^3 - c - \gamma\nabla^2 c + S) \tag{42}$$

where S is the local order parameter calculated at each lattice site in a 3D bulk.

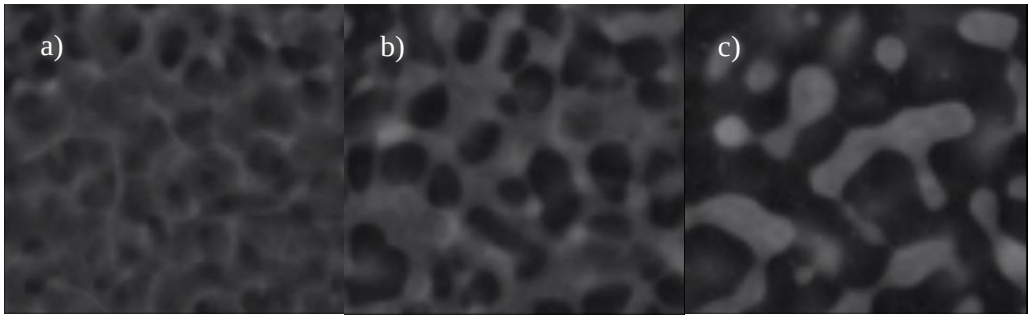

Figure 36: Snapshots of a quantum dot – doped liquid crystal going through the phase transition. The bright areas are the fluorescent quantum dot – rich isotropic areas. Note the shrinking domains as the particles begin to arrest. Snapshots are from Reference 47.

The cooling rate of the system was varied by changing the number of timesteps of the simulation. The temperature was started above the isotropic-nematic phase transition (for our system that was T = 2.0) and cooled to a temperature below the transition. The number of simulation steps ranged from 1000 timesteps for the fastest cooling rate to 10000 timesteps for the slowest cooling rate. Results for each cooling rate were averaged over 5 runs.

5.4 Results

Results for the simulation are shown in Figure 37. Figure 37a shows a slice of a bulk nematic material. Both nematic alignment and topological defects are present. In this slice, directors that seem to disappear are pointing in and out of the plane. Figure 37b shows the corresponding order map where the scalar order parameter was calculated at each lattice site. Figure 37c shows the Cahn Hilliard result. Note there is an excellent correspondence between areas of low order and the red species (the quantum dot – rich phase).

The effect of cooling rate on domain size is shown in Figure 37. Domain sizes are computed using a correlation function

$$g(r) = < c(r)c(0) > - < c >^2 \tag{43}$$

and the domain size is taken as the first zero of the correlation function. The first zero is obtained by fitting the correlation data to a polynomial [80]. The behavior of isotropic domains shrinking and following areas of low order are is recovered successfully. The data shows a linear decrease in domain size as cooling rate is increased.

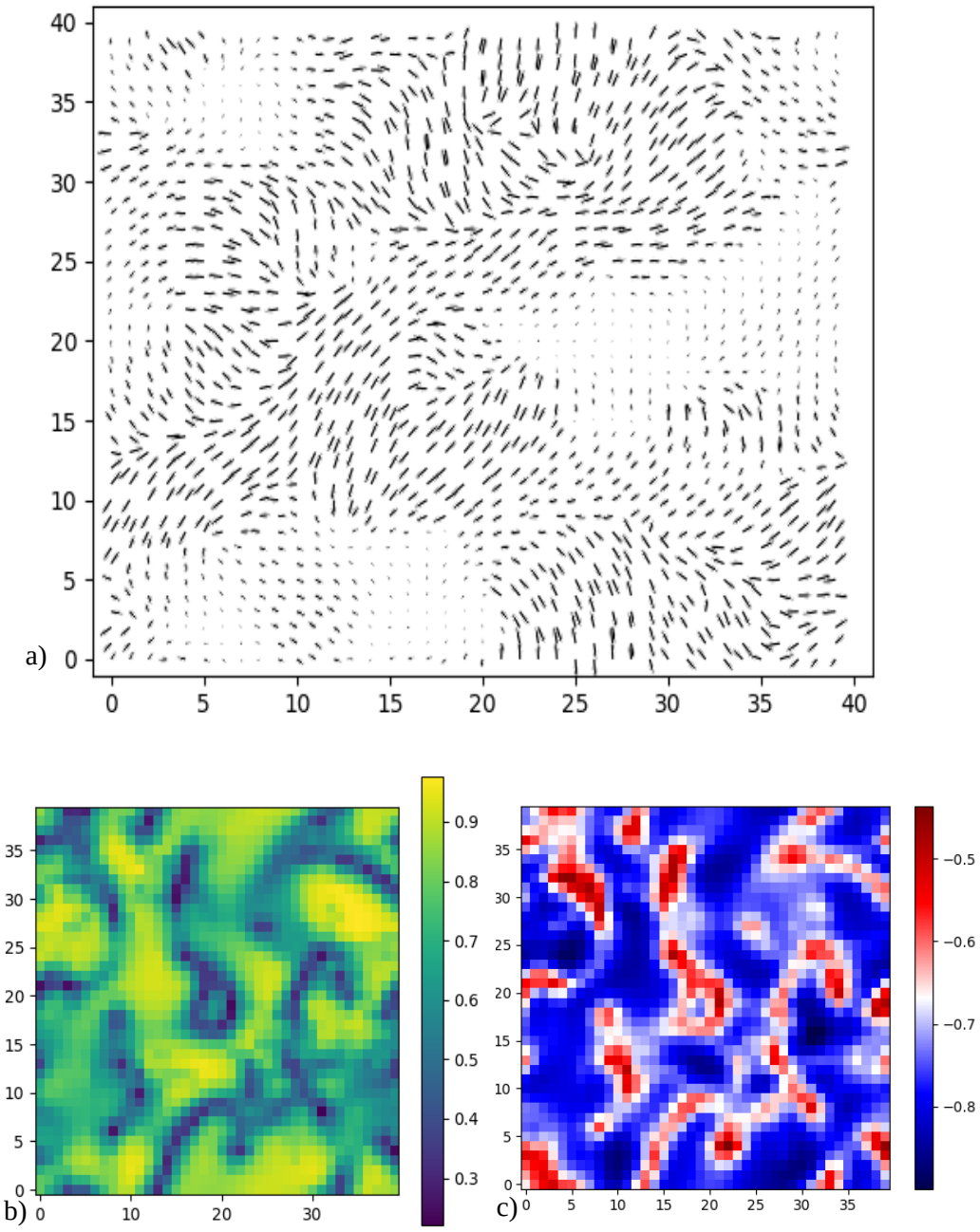

Figure 37: a) shows the director field in a slice of the bulk liquid crystal. b) is the map of the order parameter for this slice, and c) is the result of the order parameter – driven Cahn Hilliard equation.

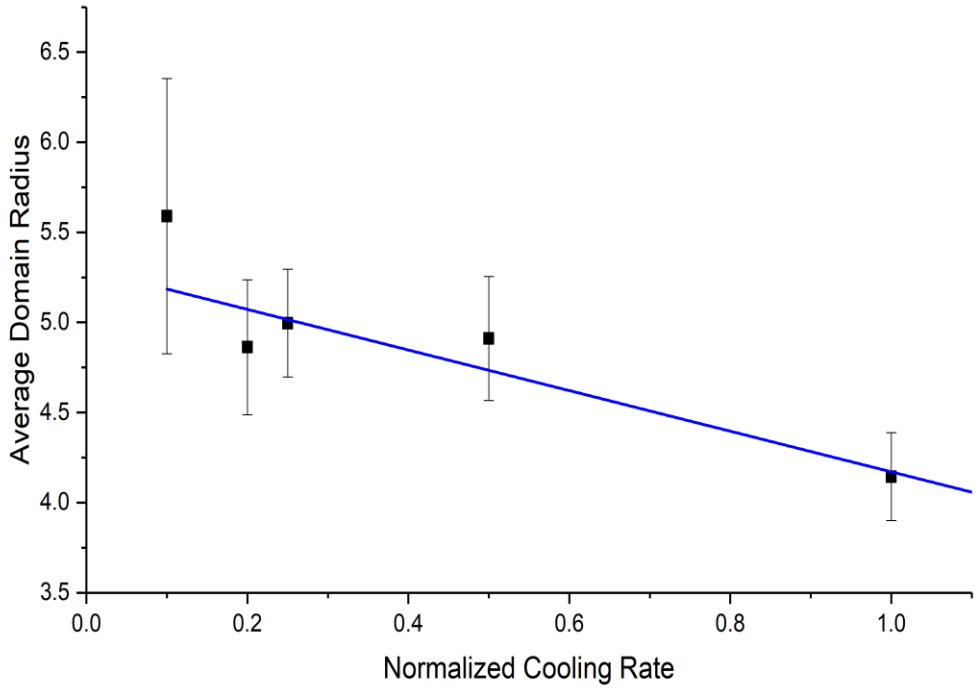

Figure 38: Domain size as a function of cooling rate.

5.5 Discussion

The proposed simulation successfully modeled particle-rich isotropic domains following areas of low order in a liquid crystal undergoing the isotropic-nematic phase transition. By varying the cooling rate of the liquid crystal, average domain size was shown to follow a linear decreasing trend. Of note, however, is the large error in the size of the slowest cooling rate.

This error is attributed to the lack coupling between nematic alignment and local concentration of particle density. In the development of Equation 42, only the driving force of the nematic order was considered. In practice, a high number of particles in a region of liquid crystal will affect the isotropic-nematic transition temperature and thus effect how well the area will align. It was determined that if the system happened to nucleate slowly, this resulted in smaller domains, and if the system nucleated quickly, this resulted in larger domains. If the system nucleates slowly, there are many disinclination lines running through the bulk, so

there exist regions where the particle-rich domains will gather and spread out. A quick nucleation event will result in very few areas of low order for the particles to gather, so they will all gather in a minimal amount of areas.

To account for this needed coupling between nematic alignment and particle concentration, a new Hamiltonian has been developed that follows a Q-tensor formalism. This new formalism incorporates elastic energy, Landau energy, the coupling term, and the Cahn Hillard terms. The new Hamiltonian is given by

$$F = \frac{K}{2}(\nabla Q)^2 + \frac{a}{2}trQ^2 + \frac{b}{3}trQ^3 + \frac{k}{4}trQ^4 + \frac{3}{2}\alpha c(trQ^2) + \frac{1}{4}(c^2-1)^2 + \frac{1}{2}|\nabla c|^2 \qquad (44)$$

The coupling occurs in the fifth term, since $trQ^2 = \frac{2}{3}S^2$. Thus, there is now a direct coupling between the concentration c and the nematic ordering S. Preliminary results are shown in Figure 39. Nematic ordering and phase separation occurs, yet how they are correlated has yet to be analyzed.

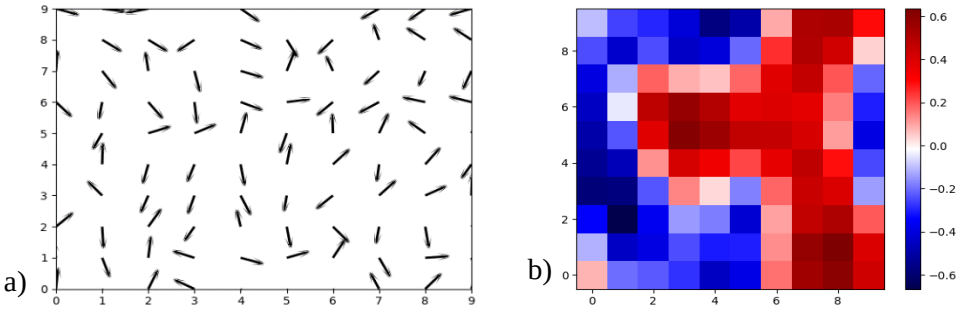

Figure 39: Preliminary simulation results of Equation 44. a) shows nematic alignment, and b) shows phase separation.

5.6 Conclusions

In conclusion a model showing both nematic alignment and phase separation in a nematic liquid crystal has been developed. Experimental results show that during the isotropic-nematic phase transition, nanoparticle-rich domains separate from nematic domains, and the size of these domains shrink in size if cooling rate of the liquid crystal is increased. The model recovers this behavior. Due to a lack of coupling between local nematic alignment and particle concentration, there is large statistical error in the slowest cooling rate regime. This is attributed to different nucleation rates in the simulation timeframe. This has been fixed by introducing a new Hamiltonian that includes this coupling, and preliminary results show promise.

References

1. Rösler, A.; Vandermeulen, G. W.; Klok, H.-A. Advanced drug delivery devices via self-assembly of amphiphilic block copolymers. *Advanced drug delivery reviews* **2001**, *53*, 95–108.

2. Yan, H.; Park, S. H.; Finkelstein, G.; Reif, J. H.; LaBean, T. H. DNA-templated self-assembly of protein arrays and highly conductive nanowires. *Science* **2003**, *301*, 1882–1884.

3. Zhang, S. Fabrication of novel biomaterials through molecular self-assembly. *Nature Biotechnology* **2003**, *21*, 1171–1178.

4. Feldheim, D.; Keating, C. Self-assembly of single electron transistors and related devices. *Chemical Society Reviews* **1998**, *27*, 1–12.

5. Whitesides, G.; Gryzbowski, B. Self-assembly at all scales. *Science* **2002**, *295*, 2418-2412.

6. Park, N. M.; Kim, T. S.; Park, S. J. Band gap engineering of amorphous silicon quantum dots for light-emitting diodes. *Appl. Phys. Lett.* **2001**, *78*, 2575-2577.

7. Zhuang, L., Guo, L.; Chou, S. Y. Single-electron transistors based on self-assembled silicon-on-insulator quantum dots. *Appl. Phys. Lett.* **1988**, *72*, 1205.

8. Jaiswal, J. K.; Mattoussi, H.; Mauro, J. M.; Simon, S. M. Long-term multiple color imaging of live cells using quantum dots bioconjugates. *Nat. Biotechnol.* **2003**, *21*, 47-51.

9. Cota-Fernandez, J. M.; Pereiro, R.; Sanz-Medal, A. The use of luminescent quantum dots for optical sensing. *TrAC*, **2006**, *23*, 207-218.

10. Nozik, A. J. Quantum dot solar cells. *Physica E*, **2002**, *14*, 954-958.

11. Blanc, C.; Coursault, D.; Lacaze, E. Ordering nano- and microparticle assemblies with liquid crystals. *Liquid Crystals Reviews* **2013**, *1*, 83–109.

12. Hegmann, T.; Qi, H.; Marx, V. M. Nanoparticles in Liquid Crystals: Synthesis, Self-Assembly, Defect Formation and Potential Applications. *J Inorg. Organomet. Polym.* **2007**, *17*, 483–508.

13. Wang, X.; Miller, D. S.; Bukusoglu, E.; de Pablo, J. J.; Abbott, N. L. Topological defects in liquid crystals as templates for molecular self-assembly. *Nat. Mater* **2016**, *15*, 106–112.

14. Glotzer, S. C.; Solomon, M. J.; Kotov, N. A. Self-assembly: From nanoscale to microscale colloids. *AIChE Journal* **2004**, *50*, 2978–2985.

15. Bigioni, T. P.; Lin, X.-M.; Nguyen, T. T.; Corwin, E. I.; Witten, T. A.; Jaeger, H. M. Kinetically driven self assembly of highly ordered nanoparticle monolayers. *Nat. Mater* **2006**, *5*, 265–270.

16. Hirst, L. S. Fundamentals of Soft Matter Science. CRC Press, Florida, **2012**.

17. Škarabot, M.; Ravnik, M.; Žumer, S.; Tkalec, U.; Poberaj, I.; Babič, D.; Muševič, I. Hierarchical self-assembly of nematic colloidal superstructures. *Physical Review E* **2008**, *77*.

18. Ramaswamy, S.; Nityananda, R.; Raghunathan, V. A.; Prost, J. Power-Law Forces Between Particles in a Nematic. *Molecular Crystals and Liquid Crystals Science* **1996**, *288*, 175–180.

19. Muševič, I.; Škarabot, M.; Tkalec, U.; Ravnik, M.; Žumer, S. Two-Dimensional Nematic Colloidal Crystals Self-Assembled by Topological Defects. *Science* **2006**, *313*, 954–958.

20. Poulin, P.; Weitz, D. A. Inverted and multiple nematic emulsions. *Phys. Rev. E* **1998**, *57*, 626.

21. Yada, M.; Yamamoto, J.; Yokoyama, H. Spontaneous formation of regular defect array in water-in-cholesteric liquid crystal emulsions. *Langmuir* **2002**, *18*, 7436–7440.

22. Urban, J. J.; Talapin, D. V.; Shevchenko, E. V.; Murray, C. B. Self-Assembly of PbTe Quantum Dots into Nanocrystal Superlattices and Glassy Films. *J. Am. Chem. Soc.* **2006**, *128*, 3248–3255.

23. Yuan, J.; Hira, S. M.; Strouse, G. F.; Hirst, L. S. Lipid Bilayer Discs and Banded Tubules: Photoinduced Lipid Sorting in Ternary Mixtures. *Journal of the American Chemical Society* **2008**, *130*, 2067–2072.

24. Quinten, M.; Leitner, A.; Krenn, J. R.; Aussenegg, F. R. Electromagnetic energy transport via linear chains of silver nanoparticles. *Opt. Lett* **1998**, *23*, 1331–1333.

25. Singh, G.; Fisch, M.; Kumar, S. Emissivity and electrooptical properties of semiconducting quantum dots/rods and liquid crystal composites: a review. *Rep. Prog. Phys* **2016**, *79*, 056502.

26. Helfrich, W.; Schadt, M. Voltage-dependent optical activity of a twisted nematic liquid crystal. In *Crystals That Flow*; Stegemeyer, H., Sluckin, T., Dunmur, D., Eds.; CRC Press, 2004; Vol. 2, pp. 537–541 ISBN 978-0-415-25789-3.

27. Chandrasekhar, S.; Sadashiva, B. K.; Suresh, K. A. Liquid crystals of disc-like molecules. *Pramana* **1977**, *9*, 471–480.

28. Wu, S.-T.; Efron, U.; Hess, L. D. Birefringence measurements of liquid crystals. *Applied Optics* **1984**, *23*, 3911.

29. Seo, D.; Iimura, Y.; Kobayashi, S. Temperature dependence of the polar anchoring strength of weakly rubbed polyimide films for the nematic liquid crystal (5CB). *Applied Physics Letters* **1992**, *61*, 234–236.

30. Chaikin, P. M.; Lubensky, T. C. *Principles of Condensed Matter Physics*, 1st ed.; Cambridge University Press: University Printing House, Cambridge CB2 8BS, United Kingdom, 1995; ISBN 0-521-43224-3.

31. Gibbons, W. M.; Shannon, P. J.; Sun, S.-T.; Swetlin, B. J. Surface-mediated alignment of nematic liquid crystals with polarized laser light. *Nature* **1991**, *351*, 49.

32. Schiekel, M. F.; Fahrenschon, K. Deformation of Nematic Liquid Crystals with Vertical Orientation in Electrical Fields. *Applied Physics Letters* **1971**, *19*, 391–393.

33. Nose, T.; Sato, S. A liquid crystal microlens obtained with a non-uniform electric field. *Liquid Crystals* **1989**, *5*, 1425–1433.

34. Quint, M. T.; Delgado, S.; Paredes, J. H.; Nuno, Z. S.; Hirst, L. S.; Ghosh, S. All-optical switching of nematic liquid crystal films driven by localized surface plasmons. *Optics Express* **2015**, *23*, 6888.
.
35. Brody, T. P.; Asars, J. A.; Dixon, G. D. A 6 #215; 6 inch 20 lines-per-inch liquid-crystal display panel. *IEEE Transactions on Electron Devices* **1973**, *20*, 995–1001, doi:10.1109/T-ED.1973.17780.

36. Lagerwall, J. P. F.; Giesselmann, F. Current Topics in Smectic Liquid Crystal Research. *ChemPhysChem* **2006**, *7*, 20–45.

37. Zheng, Z.; Li, Y.; Bisoyi, H. K.; Wang, L.; Bunning, T. J.; Li, Q. Three-dimensional control of the helical axis of a chiral nematic liquid crystal by light. *Nature* **2016**, *531*, 352–356.

38. Humar, M.; Muševič, I. 3D microlasers from self-assembled cholesteric liquid-crystal microdroplets. *Optics Express* **2010**, *18*, 26995.

39. Chen, L.; Li, Y.; Fan, J.; Bisoyi, H. K.; Weitz, D. A.; Li, Q. Photoresponsive Monodisperse Cholesteric Liquid Crystalline Microshells for Tunable Omnidirectional Lasing Enabled by a Visible Light-Driven Chiral Molecular Switch. *Advanced Optical Materials* **2014**, *2*, 845–848.

40. Poulin, P.; Stark, H.; Lubensky, T. C.; Weitz, D. A. Novel Colloidal Interactions in Anisotropic Fluids. *Science* **1997**, *275*, 1770–1773.

41. Fleury, J.-B.; Pires, D.; Galerne, Y. Self-Connected 3D Architecture of Microwires. *Phys. Rev. Lett.* **2009**, *103*.

42. Coursault, D.; Grand, J.; Zappone, B.; Ayeb, H.; Lévi, G.; Félidj, N.; Lacaze, E. Linear Self-Assembly of Nanoparticles Within Liquid Crystal Defect Arrays. *Adv. Mater* **2012**, *24*, 1461–1465.

43. Rodarte, A. L.; Pandolfi, R. J.; Ghosh, S.; Hirst, L. S. Quantum dot/liquid crystal composite materials: self-assembly driven by liquid crystal phase transition templating. *J. Mater. Chem. C* **2013**, *1*, 5527.

44. Guo, Y.; Jiang, M.; Peng, C.; Sun, K.; Yaroshchuk, O.; Lavrentovich, O.; Wei, Q.-H. High-Resolution and High-Throughput Plasmonic Photopatterning of Complex Molecular Orientations in Liquid Crystals. *Adv. Mater* **2016**, *28*, 2353–2358.

45. Frank, F. C. I. Liquid crystals. On the theory of liquid crystals. *Discussions of the Faraday Society* **1958**, *25*, 19.

46. Rodarte, A. L.; Nuno, Z. S.; Cao, B. H.; Pandolfi, R. J.; Quint, M. T.; Ghosh, S.; Hein, J. E.; Hirst, L. S. Tuning Quantum-Dot Organization in Liquid Crystals for Robust Photonic Applications. *Chem. Phys. Chem.* **2014**, *15*, 1413–1421.

47. Rodarte, A. L.; Cao, B. H.; Panesar, H.; Pandolfi, R. J.; Quint, M.; Edwards, L.; Ghosh, S.; Hein, J. E.; Hirst, L. S. Self-assembled nanoparticle micro-shells templated by liquid crystal sorting. *Soft Matter* **2015**, *11*, 1701–1707.

48. Quint, M. T.; Sarang, S.; Quint, D. A.; Keshavarz, A.; Stokes, B. J.; Subramaniam, A. B.; Huang, K. C.; Gopinathan, A.; Hirst, L. S.; Ghosh, S. Plasmon-Actuated Nano-Assembled Microshells. *Sci. Rep.* **2017**.

49. Riahinasab, S. T.; Elbaradei, A.; Keshavarz, A.; Stokes, B. J.; Hirst, L. S. Nanoparticle Microstructures Templated by Liquid Crystal Phase-Transition Dynamics, *Proc. SPIE* **2017**, 10125, 1012503-1012503-7.

50. Brasselet, E.; Murazawa, N.; Misawa, H.; Juodkazis, S. Optical Vortices from Liquid Crystal Droplets. *Physical Review Letters* **2009**, *103*.

51. Fan, J.; Li, Y.; Bisoyi, H. K.; Zola, R. S.; Yang, D.; Bunning, T. J.; Weitz, D. A.; Li, Q. Light-Directing Omnidirectional Circularly Polarized Reflection from Liquid-Crystal Droplets. *Angew. Chem. Int. Ed.* **2015**, *54*, 2160–2164.

52. Kim, J.; Khan, M.; Park, S.-Y. Glucose Sensor using Liquid-Crystal Droplets Made by Microfluidics. *ACS Applied Materials & Interfaces* **2013**, *5*, 13135–13139.

53. Seč, D.; Porenta, T.; Ravnik, M.; Žumer, S. Geometrical frustration of chiral ordering in cholesteric droplets. *Soft Matter* **2012**, *8*, 11982.

54. Lopez-Leon, T.; Fernandez-Nieves, A. Drops and shells of liquid crystal. *Colloid and Polymer Science* **2011**, *289*, 345–359.

55. Lopez-Leon, T.; Koning, V.; Devaiah, K. B. S.; Vitelli, V.; Fernandez-Nieves, A. Frustrated nematic order in spherical geometries. *Nature Physics* **2011**, *7*, 391–394.

56. Doane, J. W.; Vaz, N. A.; Wu, B. -G.; Žumer, S. Field controlled light scattering from nematic microdroplets. *Applied Physics Letters* **1986**, *48*, 269–271.

57. Drzaic, P. S. Polymer dispersed nematic liquid crystal for large area displays and light valves. *Journal of Applied Physics* **1986**, *60*, 2142–2148.

58. Coates, D. Polymer-dispersed Liquid Crystals. *J. MATER. CHEM.* **1995**, *5*, 10.

59. Fernández-Nieves, A.; Link, D. R.; Márquez, M.; Weitz, D. A. Topological Changes in Bipolar Nematic Droplets under Flow. *Phys. Rev, Lett.* **2007**, *98*.

60. Wang, X.; Miller, D. S.; de Pablo, J. J.; Abbott, N. L. Organized assemblies of colloids formed at the poles of micrometer-sized droplets of liquid crystal. *Soft Matter* **2014**, *10*, 8821–8828.

61. Whitmer, J. K.; Wang, X.; Mondiot, F.; Miller, D. S.; Abbott, N. L.; de Pablo, J. J. Nematic-Field-Driven Positioning of Particles in Liquid Crystal Droplets. *Phys. Rev. Lett.* **2013**, *111*.

62. Selinger, R. L. B.; Konya, A.; Travesset, A.; Selinger, J. V. Monte Carlo Studies of the XY Model on Two-Dimensional Curved Surfaces. *J. Phys. Chem. B* **2011**, *115*, 13989–13993.

63. Hirst, L. S.; Ossowski, A.; Fraser, M.; Geng, J.; Selinger, J. V.; Selinger, R. L. B. Morphology transition in lipid vesicles due to in-plane order and topological defects. *PNAS* **2013**, *110*, 3242–3247.

64. Bradač, Z.; Kralj, S.; Žumer, S. Early stage domain coarsening of the isotropic-nematic phase transition. *J. Chem. Phys.* **2011**, *135*, 024506.

65. Sengupta, A. Liquid Crystal Theory. In *Topological Microfluidics*; Springer International Publishing: Cham, 2013; pp. 7–36 ISBN 978-3-319-00857-8.

66. Selinger, J. V. *Introduction to the Theory of Soft Matter*; Soft and Biological Matter; Springer International Publishing: Cham, 2016; ISBN 978-3-319-21053-7.

67. Lee, T. D.; Yang, C. N. Statistical Theory of Equations of State and Phase Transitions. II. Lattice Gas and Ising Model. In *Selected Papers*; Feinberg, G., Ed.; Birkhäuser Boston: Boston, MA, 1986; pp. 535–544 ISBN 978-1-4612-5399-0.

68. Deem, M. W. Disclination asymmetry in two-dimensional nematic liquid crystals with unequal Frank constants. *Physical Review E* **1996**, *54*, 6441–6451.

69. Shin, H.; Bowick, M. J.; Xing, X. Topological Defects in Spherical Nematics. *Phys. Rev. Lett.* **2008**, *101*.

70. Lebwohl, P. A.; Lasher, G. Nematic-Liquid-Crystal Order-A Monte Carlo Calculation. *Physical Review A* **1973**, *7*, 2222–2222.

71. Chukwuocha, E. O.; Onyeaju, M. C.; Harry, T. S. T. Theoretical Studies on the Effect of Confinement on Quantum Dots Using the Brus Equation. *World Journal of Condensed Matter Physics* **2012**, *02*, 96–100.

72. Amaral, J. J.; Wan, J.; Rodarte, A. L.; Ferri, C.; Quint, M. T.; Pandolfi, R. J.; Scheibner, M.; Hirst, L. S.; Ghosh, S. Magnetic field induced quantum dot brightening in liquid crystal synergized magnetic and semiconducting nanoparticle composite assemblies. *Soft Matter* **2015**, *11*, 255–260.

73. Diez, S.; Dunmur, D. A.; Rosario De La Fuente, M.; Karahaliou, P. K.; Mehl, G.; Meyer, T.; Ángel PerÉz Jubindo, M.; Photinos, D. J. Dielectric studies of a laterally-linked siloxane ester dimer. *Liquid Crystals* **2003**, *30*, 1021–1030.

74. Prodanov, M. F.; Pogorelova, N. V.; Kryshtal, A. P.; Klymchenko, A. S.; Mely, Y.; Semynozhenko, V. P.; Krivoshey, A. I.; Reznikov, Y. A.; Yarmolenko, S. N.; Goodby, J. W.; Vashchenko, V. V. Thermodynamically Stable Dispersions of Quantum Dots in a Nematic Liquid Crystal. *Langmuir* **2013**, *29*, 9301–9309.

75. Eggersdorfer, M. L.; Pratsinis, S. E. Agglomerates and aggregates of nanoparticles made in the gas phase. *Advanced Powder Technology* **2014**, *25*, 71–90.

76. Botet, R.; Jullien, R. Intrinsic anisotropy of clusters in cluster-cluster aggregation. *Journal of Physics A: Mathematical and General* **1986**, *19*, L907.

77. Qiao, X.; Zhang, X.; Guo, Y.; Yang, S.; Tian, Y.; Meng, Y. Boundary layer viscosity of CNT-doped liquid crystals: effects of phase behavior. *Rheologica Acta* **2013**, *52*, 939–947.

78. Elliott, C. M.; French, D. A. Numerical Studies of the Cahn-Hilliard Equation for Phase Separation. *IMA Journal of Applied Mathematics* **1987**, *38*, 97–128.

79. Pinto, Vianney Karian Giminez. Modeling Liquid Crystal Polymeric Devices. PhD Thesis. **2004**, Kent State Univeristy.

80. Sappelt, D.; Jäckle, J. Computer simulation study of phase separation in a binary mixture with a glass-forming component. *Physica A: Statistical Mechanics and its Applications* **1997**, *240*, 453–479.